J. Fluid Mech. (2022), *vol*. 932, A38, doi:10.1017/jfm.2021.1026

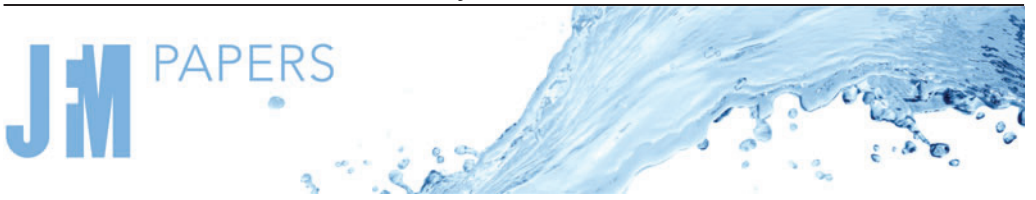

The effect of tidal force and topography on horizontal convection

Guang-Yu Ding[1,2], **Yu-Hao He**[1,2] **and Ke-Qing Xia**[1,2,3,†]

[1]Center for Complex Flows and Soft Matter Research and Department of Mechanics and Aerospace Engineering, Southern University of Science and Technology, Shenzhen 518055, PR China

[2]Department of Physics, The Chinese University of Hong Kong, Hong Kong, PR China

[3]Guangdong Provincial Key Laboratory of Turbulence Research and Applications, Southern University of Science and Technology, Shenzhen 518055, PR China

(Received 25 February 2021; revised 27 October 2021; accepted 14 November 2021)

We present a numerical study on how tidal force and topography influence flow dynamics, transport and mixing in horizontal convection. Our results show that local energy dissipation near topography will be enhanced when the tide is sufficiently strong. Such enhancement is related to the height of the topography and increases as the tidal frequency ω decreases. The global dissipation is found to be less sensitive to the changes in ω when the latter becomes small and asymptotically approaches a constant value. We interpret the behaviour of the dissipation as a result of the competition among the dominant forces in the system. According to which mechanism prevails, the flow state of the system can be divided into three regimes, which are the buoyancy-, tide- and drag-control regimes. We show that the mixing efficiency η for different tidal energy and topography height can be well described by a universal function $\eta \approx \eta_{HC}/(1+\mathcal{R})$, where η_{HC} is the mixing efficiency in the absence of tide and $\mathcal{R}$ is the ratio between tidal and available potential energy inputs. With this, one can also determine the dominant mechanism at a certain ocean region. We further derive a power law relationship connecting the mixing coefficient and the tidal Reynolds number.

Key words: buoyancy-driven instability, topographic effects, mixing and dispersion

1. Introduction

The meridional overturning circulation (MOC) plays a crucial role in the Earth's climate and energy system. Candidates of the energy sources sustaining the MOC include mechanical forcing (e.g. wind and tide), thermal forcing at the ocean surface, geothermal heating and so forth (Munk 1966; Whitehead 1995; Wunsch 2000;

† Email address for correspondence: xiakq@sustech.edu.cn

Wunsch & Ferrari 2004). Among these sources, the mechanical forcing has been widely accepted as an important contributor (wind and tide individually contribute approximately 1 TW, see Wunsch 2000; Wunsch & Ferrari 2004). Geothermal heating is important for the abyssal stratification and circulation strength (Scott, Marotzke & Adcroft 2001; Mashayek *et al.* 2013; Wang *et al.* 2016), but its contribution to the meridional heat flux is relatively weak (0.05 TW, see Huang 1999; Wunsch & Ferrari 2004). As for surface thermal forcing, its quantitative contribution to the energy budget of the MOC has been debated for decades but remains an open question. One of the criticisms about surface thermal forcing is its weak contribution to the global oceanic energy budgets ($\approx$1.5 GW Wang & Huang 2005). Such an amount is even smaller than that of geothermal heating. For this reason, it was inferred that surface thermal forcing alone cannot sustain the turbulence level and the amount of viscous dissipation observed in the ocean (Paparella & Young 2002; Wang & Huang 2005). A recent experiment conducted by Wang, Huang & Xia (2018) supports this argument, and suggests that surface thermal forcing is less vital than the mechanical sources for the MOC. However, the study conducted by Hughes, Hogg & Griffiths (2009) indicated that the importance of surface thermal forcing is reflected in terms of its contribution in generating available potential energy and maintaining irreversible diapycnal mixing, rather than producing interior viscous dissipation and the oceanic kinetic energy. This suggests that the available potential energy generated by surface thermal forcing and the kinetic energy provided by the mechanical forcing are both necessary to maintain the overturning circulation. Although there still lacks consensus on the exact role played by surface thermal forcing in the ocean, it is obvious that the MOC is not driven by a single force and it must be a system with multiple driving mechanisms. As suggested by Saenz *et al.* (2012), mechanical and thermal forcing can act in a concerted way, which means that the contribution of thermal forcing can be significantly affected by the mechanical forcing. Thus, examining the different mechanisms separately may lead to incorrect estimations of their respective contributions. Rather than comparing different types of forcing in an isolated way, investigation of a system with multiple controllable energy inputs would help to better understand the dynamics of the MOC.

As one of the main mechanical sources, wind shearing was compared with surface thermal forcing in some recent studies (Hazewinkel, Paparella & Young 2012; Saenz *et al.* 2012; Sohail, Gayen & Hogg 2018). Another main mechanical source is the tide. Unlike the wind shearing that mainly affects the upper ocean, the tide is a body mechanism that acts on the whole system. The interaction between tide and topography is widely believed to play a key role in hydrodynamic process of the ocean interior (Lamb 2014; Sarkar & Scotti 2017). A rough topography is a site of internal wave generation (Egbert & Ray 2000; Nycander 2005; Garrett & Kunze 2007), where enhanced turbulent mixing has been observed (Polzin *et al.* 1997; Ledwell *et al.* 2000; Heywood, Naveira Garabato & Stevens 2002). A recent study conducted by Waterhouse *et al.* (2014) compiles a set of turbulent mixing data measured in diverse oceanic regimes and reveals that over rough or abrupt ridge topography, the dissipation rate is enhanced compared with that over a smooth bottom. Between these two kinds of topographies, the ridge case yields stronger enhancement than the rough one, which implies that the height of the topography also has a significant influence on the dissipation rate. To the best of our knowledge, direct comparative studies between thermal and tidal forcings are rare.

To have a better understanding of the interaction between different mechanisms in the real ocean, studies of idealized models will be a very useful complementary approach. In this study, we use an idealized model to investigate the coupling effect of surface thermal forcing and tidal forcing, and directly compare their respective contributions to the

energy budgets of our model system. The model we used in this study is called horizontal convection (HC), which is an important paradigm modelling the effect of surface thermal forcing. In this model, fluid motion is driven by the surface temperature difference applied horizontally on a fluid layer (Rossby 1965; Killworth & Manins 1980; Mullarney, Griffiths & Hughes 2004; Hughes & Griffiths 2008; Shishkina, Grossmann & Lohse 2016; Wang *et al.* 2016, 2018). Given the intimate connection between tidal force and topography in the real ocean, we also investigate the effect of topography on this system. Our study supports the argument that mechanical and thermal forcings act in a coupled way (Saenz *et al.* 2012). We observe dissipation enhancement when the tidal effect is sufficiently strong. Such enhancement is related to the height of the topography. We further extract the tidal energy input from the global dissipation, and separate the flow strengths attributable to different mechanisms. According to these results, we identify three flow regimes corresponding to different control mechanisms, which are buoyancy-, tide- and drag-control. Heat transfer enhancement is also observed once the system enters the tide-control regime. In addition, a universal relation on mixing efficiency is derived, which reveals that the mixing efficiency can be expressed as a function of the ratio between tidal and available potential energy inputs. We stress that the current study is based on an idealized model in the absence of some important forces present in the ocean, like the Coriolis force and surface wind shearing. As a result, many dynamic features such as flow structures in this system may be noticeably different from those observed in the ocean. Nevertheless, with the above caveat in mind, the results, such as the energy budgets, regime divisions and the universal relation for mixing efficiency, may provide insights for understanding the dynamics of the MOC.

The remainder of this paper is organized as follows. Section 2 introduces the flow set-up and numerical method used in this study. Section 3 briefly reviews the energy pathway in an HC system with tidal energy input. Section 4 presents the results and discussion related to the global energy. In § 4.1, results of the volume integral of viscous dissipation are shown and discussed. In § 4.2, the tidal energy input is extracted from global dissipation, showing how the tidal force contributes to the global energy. According to the result of tidal energy input, the drag-control regime is first identified. Section 4.3 presents the results of the flow strength corresponding to different mechanisms, and tide- and buoyancy-control regimes are then identified. In § 4.4, we present the results of global heat transfer and discuss the transition from the buoyancy-control regime to the tide-control one. In § 4.5, we discuss the energy dissipation profiles measured at different regions and under various topographies and tidal frequencies. In § 4.6, we show the stratification profiles and flow patterns for different tidal frequencies. Section 4.7 presents and discusses the mixing efficiency. We show that the mixing efficiency can be expressed as a function of the ratio between tidal power and the generation rate of the available potential energy. According to this result, we further develop a relation connecting the mixing efficiency and the tidal velocity. In § 5, we summarize and conclude the present study.

2. Numerical method and governing equations

In this study, we conduct direct numerical simulations (DNSs) with tidal force and topography. To explore the wide range of tidal frequencies in this study, the majority of our simulations are two-dimensional. To ensure that the features we observed in two-dimensional simulations are representative and can be applied to three-dimensional situations, we also conduct a series of three-dimensional simulations for comparison. As can be seen below, the two- and three-dimensional results are consistent with each other. As illustrated in figure 1, we consider a body of fluid (water in the present case) with

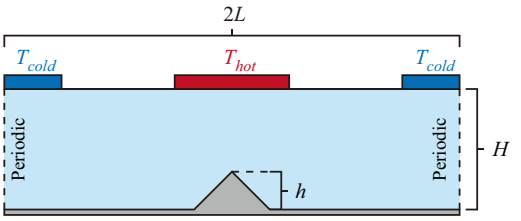

Figure 1. Illustrations of the numerical set-up. Hot plate with length $2\lambda L$ is located at the top centre, and cold plates with length λL are placed at the top two ends of the cell. The periodic boundary condition is applied at the two lateral boundaries.

non-slip isothermal hot and cold plates, with temperatures T_{hot} and T_{cold}, respectively, located at the top. The normalized total area of the hot and cold plates is denoted as $\lambda = L_{hot}/(2L) = L_{cold}/(2L)$, which equals to 0.2 in all our simulations, where L is the half-length of the convective cell. The boundaries at the top surface and between these plates are adiabatic and shear-free. All lateral boundaries are periodic and the bottom is adiabatic and no-slip. A triangular topography with height h and width $2h$ is placed at the centre of the bottom boundary, directly below the hot plate. Physical quantities are non-dimensionalized by $x_{ref} = L$, $u_{ref} = (\alpha g L \Delta)^{1/2}$, $T_{ref} = \Delta$ and $t_{ref} = x_{ref}/u_{ref}$, where α is the thermal expansion coefficient, g the gravitational acceleration, and $\Delta = T_{hot} - T_{cold}$ is the temperature difference between hot and cold plates. The system is governed by dimensionless Navier–Stokes equations in Oberbeck–Boussinesq approximation:

$$\boldsymbol{\nabla} \cdot \boldsymbol{u} = 0, \tag{2.1a}$$

$$\frac{\partial \boldsymbol{u}}{\partial t} + \boldsymbol{u} \cdot \boldsymbol{\nabla} \boldsymbol{u} = -\boldsymbol{\nabla} p + \sqrt{\frac{Pr}{Ra}} \nabla^2 \boldsymbol{u} + \theta \boldsymbol{e_z} + A \sin(\omega t) \boldsymbol{e_x}, \tag{2.1b}$$

$$\frac{\partial \theta}{\partial t} + \boldsymbol{u} \cdot \boldsymbol{\nabla} \theta = \frac{1}{\sqrt{RaPr}} \nabla^2 \theta, \tag{2.1c}$$

where u, p and $\theta = [T - (T_{hot} + T_{cold})/2]/\Delta$ are the dimensionless velocity, pressure and reduced temperature, respectively. A periodic tidal force $A \sin(\omega t) \boldsymbol{e_x}$ is applied to the system horizontally, where A and ω are the non-dimensional tidal force amplitude and frequency, respectively. There are another two dimensionless control parameters of this system: $Ra = \alpha g \Delta L^3/(\kappa \nu)$ is the Rayleigh number representing the strength of thermal driving, and $Pr = \nu/\kappa$ is the ratio between momentum and thermal diffusivity of the working fluid. Here, ν refers to the kinetic viscosity and κ the thermal diffusivity. The geometrical properties of the convective cell is described by the aspect ratio $\Gamma \equiv H/L$, where H is the height of the convective cell. In our simulations, we fix $A = 1 \times 10^{-3}$, $Ra = 1 \times 10^{10}$, $Pr = 8.0$ and $\Gamma = 0.2$, and ω ranges from 1 to 1×10^{-3}. For three-dimensional simulations, the width of the convection cell is fixed to be $W/L = 0.1$. For each topography, a simulation without tidal force is conducted for comparison. The governing parameters in this study are summarized in table 1.

Governing equations (2.1) are solved by a well-tested DNS code called CUPS (Kaczorowski & Xia 2013; Kaczorowski, Chong & Xia 2014; Chong, Ding & Xia 2018), which is based on the finite volume method and achieves fourth-order spatial precision. Temperature and velocity fields are discretized in staggered grids. The simulations with topography are achieved by applying the immersed boundary method (IBM) (Fadlun *et al.* 2000). In the IBM scheme, solid boundaries are considered as a 'freezed' fluid

No.	h/H	A	ω		No.	h/H	A	ω	
1	0	0	—	2-D	25	0.5	0	—	2-D
2	0	1×10^{-3}	1	2-D	26	0.5	0	—	3-D
3	0	1×10^{-3}	0.8	2-D	27	0.5	1×10^{-3}	0.4	2-D
4	0	1×10^{-3}	0.4	2-D	28	0.5	1×10^{-3}	0.1	2-D
5	0	1×10^{-3}	0.2	2-D	29	0.5	1×10^{-3}	0.1	3-D
6	0	1×10^{-3}	0.14	2-D	30	0.5	1×10^{-3}	0.06	2-D
7	0	1×10^{-3}	0.12	2-D	31	0.5	1×10^{-3}	0.04	2-D
8	0	1×10^{-3}	0.1	2-D	32	0.5	1×10^{-3}	0.04	3-D
9	0	1×10^{-3}	0.0705	2-D	33	0.5	1×10^{-3}	0.02	2-D
10	0	1×10^{-3}	0.06	2-D	34	0.5	1×10^{-3}	0.01	2-D
11	0	1×10^{-3}	0.04	2-D	35	0.5	1×10^{-3}	0.004	2-D
12	0	1×10^{-3}	0.02	2-D	36	0.5	1×10^{-3}	0.001	2-D
13	0	1×10^{-3}	0.01	2-D	37	0.75	0	—	2-D
14	0	1×10^{-3}	0.004	2-D	38	0.75	1×10^{-3}	1	2-D
15	0	1×10^{-3}	0.001	2-D	39	0.75	1×10^{-3}	0.8	2-D
16	0.25	0	—	2-D	40	0.75	1×10^{-3}	0.4	2-D
17	0.25	1×10^{-3}	0.4	2-D	41	0.75	1×10^{-3}	0.2	2-D
18	0.25	1×10^{-3}	0.1	2-D	42	0.75	1×10^{-3}	0.14	2-D
19	0.25	1×10^{-3}	0.06	2-D	43	0.75	1×10^{-3}	0.12	2-D
20	0.25	1×10^{-3}	0.04	2-D	44	0.75	1×10^{-3}	0.1	2-D
21	0.25	1×10^{-3}	0.02	2-D	45	0.75	1×10^{-3}	0.07	2-D
22	0.25	1×10^{-3}	0.01	2-D	46	0.75	1×10^{-3}	0.06	2-D
23	0.25	1×10^{-3}	0.004	2-D	47	0.75	1×10^{-3}	0.04	2-D
24	0.25	1×10^{-3}	0.001	2-D	48	0.75	1×10^{-3}	0.02	2-D
					49	0.75	1×10^{-3}	0.01	2-D
					50	0.75	1×10^{-3}	0.004	2-D
					51	0.75	1×10^{-3}	0.001	2-D

Table 1. List of control parameters in this study. Here, A is the tidal force amplitude, h/H the normalized height of topography and ω the tidal frequency. The cases with $A = 0$ refer to the simulations in the absence of tidal force. 2-D and 3-D refer to two- and three-dimensional simulation, respectively. In the current study, Ra, Pr and Γ are fixed as $Ra = 1 \times 10^{10}$, $Pr = 8.0$ and $\Gamma = 0.2$.

in the simulations. To freeze the boundaries, a virtual body force is introduced, so that the acceleration produced by the adjacent convection, pressure gradient and temperature difference is cancelled out. With the help of IBM, we use structured grids in our simulations. A 1024×256 grid is used for 2-D simulations and $1024 \times 256 \times 128$ for 3-D simulations. To ensure that small local length scales are resolved, grids are refined near boundaries and topography. We verify our simulations according to the exact relation of the global heat transfer. The global heat transfer rate of this system is represented by the Nusselt number defined as $Nu \equiv \langle \mathrm{d}T/\mathrm{d}z \rangle_{hot}/(\Delta/L) = \langle \mathrm{d}T/\mathrm{d}z \rangle_{cold}/(\Delta/L)$. Here, $\langle \cdot \rangle$ represents the averaging over space, and the subscript stands for averaging over hot and cold plates. An exact relation relating Nu and the dissipation rate of thermal variance $\epsilon_T \equiv \kappa(\nabla T)^2$ can be derived from the governing equation (2.1) and boundary conditions, i.e. $\epsilon_T = (\lambda/\Gamma)(\kappa\Delta^2/L^2)Nu$ (Wang *et al.* 2016, 2018). For all our simulations, the largest deviation of averaged Nu over either the hot or cold plates from the exact relation is less than 1.6 %, which proves the reliability of our code and results. All statistical quantities are collected only after the system has reached the thermal equilibrium state. We show two examples of the temperature times series at the bulk and in the vicinity of the topography

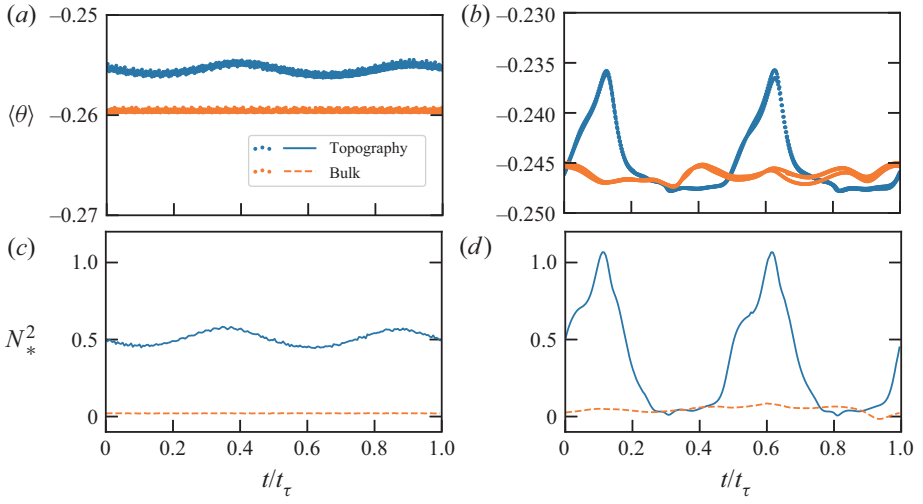

Figure 2. (*a*,*b*) Temperature series at the bulk and in the vicinity of the topography, and (*c*,*d*) N_*^2 ensemble averaged over different tidal periods as a function of t/t_τ for $h/H = 0.75$. Here, $t_\tau = 2\pi/\omega$ is the tidal period. The tidal frequency for panels (*a*,*c*) is $\omega = 0.4$ and for panels (*b*,*d*), $\omega = 0.04$. The data of temperature in panels (*a*,*b*) are resembled in one tidal cycle. The legend Topography (Bulk) refers to the results averaged over the region labelled by rectangle C (D) in figure 3(*d*).

for $h/H = 0.75$ in figure 2(*a*,*b*). The data are resembled in one tidal cycle. The times series of temperature for different tidal periods collapse together, which proves the thermal equilibrium of the system. In the rest of this paper, symbols without special notation stand for the non-dimensional quantities.

3. Energy pathway and mixing efficiency

As pointed out by Hughes *et al.* (2009), surface thermal forcing is important for maintaining the irreversible diapycnal mixing in the ocean. In the oceanographic context, mixing is generally understood as the process with irreversible changes in the scalar field that are induced by macroscopic fluid motions (Peltier & Caulfield 2003). To express mixing correctly, we need to introduce the concepts of background and available potential energies (Lorenz 1955; Winters *et al.* 1995; Winters & Young 2009). In this section, we will briefly explain the energy pathway, background and available potential energies, and mixing efficiency in this system. For generality, we discuss the three-dimensional situation in this section. The results can then be easily applied to the two-dimensional cases we mainly used in the current study. The conversion between different forms of energy is one of the key topics in the HC system. The rate of production of potential energy E_p is given by (Winters & Young 2009):

$$\phi_i = \int\int (\theta_{z=H} - \theta_{z=f_h(x,y)})\,\mathrm{d}x\,\mathrm{d}y. \tag{3.1}$$

Here, $f_h(x, y)$ is a function describing the local height of the topography. For the smooth area, $f_h = 0$. Potential energy E_p can be converted to kinetic energy E_k with the transfer rate being $\phi_z = \sqrt{RaPr}\int_V w\theta\,\mathrm{d}V$. The rate of production of potential energy E_p should equal its conversion rate to kinetic energy E_k in long time averaging, which leads to a relation $\langle\phi_i\rangle_t = \langle\phi_z\rangle_t$, where $\langle\cdot\rangle_t$ stands for the temporal averaging. Other than the

buoyancy, another source of kinetic energy E_k is the work done by the mechanical driving force, such as tidal force or shearing by surface wind. The transfer rate arising from those sources is denoted as ϕ_τ and, in the present case, is given by

$$\phi_\tau = \sqrt{RaPr} \int_V u_x A \sin(\omega t)\, \mathrm{d}V, \tag{3.2}$$

where u_x is the horizontal component of velocity. Kinetic energy E_k is maintained by the buoyancy and tidal force through ϕ_z and ϕ_τ, respectively, and dissipated through viscous dissipation $\epsilon_v = Pr \sum_i \sum_j (\partial u_i/\partial x_j)^2$. Such dissipated kinetic energy is eventually converted to internal energy. However, in most situations, the change in internal energy arising from viscous dissipation is negligibly small and is not considered in the present study. The energy balance of E_k, in an average sense, results in a relation $\langle \mathcal{E} \rangle_t = \langle \phi_\tau \rangle_t + \langle \phi_z \rangle_t$, where $\mathcal{E} \equiv \int_V \epsilon_v \, \mathrm{d}V$ is the total viscous dissipation rate. Using the balance relation for E_p, we further obtain a relation of viscous dissipation:

$$\langle \mathcal{E} \rangle_t = \langle \phi_\tau \rangle_t + \langle \phi_i \rangle_t. \tag{3.3}$$

According to its ability of doing mechanical work, potential energy E_p can be divided into background potential energy (BPE), which corresponds to the ground state that the current temperature field is redistributed to minimize the potential energy with probability density function (p.d.f.) of temperature being unchanged and available potential energy (APE) $APE \equiv E_p - BPE$, which corresponds to the portion of E_p that is available to convert to E_k through ϕ_z. The generation rate of available potential energy $G(APE)$ is given by $G(APE) \equiv NuV\lambda$. However, APE is converted to BPE when the p.d.f. of the temperature distribution is changed. Such conversion is achieved through diapycnal mixing, which is quantified by $\phi_d - \phi_i$. Here, ϕ_d is defined as $\phi_d \equiv \int_V (\mathrm{d}z^*/\mathrm{d}\theta) |\nabla\theta|^2 \, \mathrm{d}V$, where z^* is the reference position in the state of minimum potential energy of the corresponding fluid parcel (Winters *et al.* 1995; Winters & Young 2009). The statistical balance in APE then leads to a relation:

$$G(APE) = \phi_d. \tag{3.4}$$

Diapycnal mixing is considered to be an important mechanism transporting heat from the surface to the deepwater (Munk & Wunsch 1998; Wunsch & Ferrari 2004; Kuhlbrodt *et al.* 2004). The ratio between the irreversible energy transfer related to diapycnal mixing and the total energy expended is referred to as the mixing efficiency η (Peltier & Caulfield 2003; Gayen *et al.* 2013; Gregg *et al.* 2018), which is defined as

$$\eta \equiv \frac{\langle \phi_d \rangle_t - \langle \phi_i \rangle_t}{\langle \phi_d \rangle_t - \langle \phi_i \rangle_t + \langle \mathcal{E} \rangle_t} = \frac{\langle G(APE) \rangle_t - \langle \phi_i \rangle_t}{\langle G(APE) \rangle_t - \langle \phi_i \rangle_t + \langle \mathcal{E} \rangle_t}. \tag{3.5}$$

Mixing efficiency is commonly thought to be $\eta \approx 0.2$ (Peltier & Caulfield 2003; Kuhlbrodt *et al.* 2004; Wunsch & Ferrari 2004). As indicated by Kuhlbrodt *et al.* (2004), however, the magnitude of η is highly diverse between different studies or models. In the main thermocline, η is as low as 0.05 (Caldwell & Mourn 1995). However, a recent study conducted by Sohail *et al.* (2018) reports a mixing efficiency obtained from the Southern Ocean model of much greater than 0.2 and demonstrates that the global mixing efficiency is sensitive to the strength of mechanical forcing, which is wind stress in that paper. In the present study, we investigate systematically how different energy sources affect the global energy balance and mixing efficiency. For simplicity, $\langle \cdot \rangle_t$ is omitted in the following discussions.

4. Results

4.1. *Influence of topography and tidal frequency to viscous dissipation*

We first examine the flow structure and distribution of viscous dissipation when the tidal effect is sufficiently strong. Figure 3 presents the temporally averaged velocity vectors (left half) and viscous dissipation field in log scale (right half) of different topographies with $\omega = 0.04$. The normalized height of topography h/H corresponds to 0, 0.25, 0.5 and 0.75 in figure 3(*a–d*). For $h/H = 0$, we observe a large-scale circulation that downwells underneath the cold plate and upwells gradually during the horizontal movement towards the hot plate. Such mean flow structure is consistent with previous observations in horizontal convection without a tidal force (Hughes & Griffiths 2008; Shishkina 2017). As shown in figure 3(*a*), the flow strength underneath the hot plate is weak. When topography is introduced, strong flow can be observed in the area adjacent to the topography. As shown in figure 3(*c*,*d*), for $h/H = 0.5$ and $h/H = 0.75$, such strong flow near topography develops vortices that change the single-roll large-scale circulation into a multi-roll structure. Quantitatively similar flow structures (e.g. vortical flows in the vicinity of topography) and distribution of ϵ_v can be found in figure 3(*e*), which corresponds to the three-dimensional simulation with similar conditions as figure 3(*c*). Owing to the formation of the larger vortex near the topography, the local viscous dissipation ϵ_v is significantly enhanced. Such dissipation enhancement near topography agrees with field observations in the ocean interior. Previous field studies explain this enhancement as a result of the breaking of internal waves generated by a tide–topography interaction (Waterhouse *et al.* 2014). The angle of the internal wave is determined by the buoyancy frequency $N \equiv \sqrt{\alpha g(\partial\theta/\partial z)}$ and tidal frequency according to the dispersion relation (Kundu *et al.* 2016):

$$\tan\beta = \sqrt{\frac{\omega^2}{N_*^2 - \omega^2}}, \tag{4.1}$$

where β is the angle between the group velocity and the horizontal direction, and $N_* \equiv N/(1/t_{ref})$ is the dimensionless buoyancy frequency. The existence of internal waves requires $N_*/\omega > 1$ near the tip of the topography. This condition is fulfilled in many of our cases, which suggests the existence of internal waves. However, we find it difficult to extract internal wave signals in this study. One of the reasons could be that the background flow generated by the HC system absorbs the internal wave, which is understood as the result of the critical layer (Bretherton 1966). More importantly, we find that the buoyancy frequency is vertically non-uniform in our study, which bends the internal wave beam (Mathur & Peacock 2009). We also observe that the buoyancy frequency significantly varies with time, as shown in figure 2(*c*,*d*). The spatial and temporal dependence of buoyancy frequency causes the angle of internal waves to be dependent not only on the height but also on time. These difficulties together make it extremely challenging to identify internal wave signals in our system.

Nevertheless, it is clear that the tide–topography interaction induces strong local flow near topography and leads to the enhancement in local viscous dissipation. Also, as indicated by the velocity vector and local dissipation, flow strength in the area adjacent to topography is sensitive to its height. Considering the above difficulties of extracting internal waves in our system, we do not focus on the local influence and structures of internal waves. Instead, we investigate the global properties (e.g. mean viscous dissipation) and energy budgets of the system, in which the contributions of internal waves and other mechanisms are included.

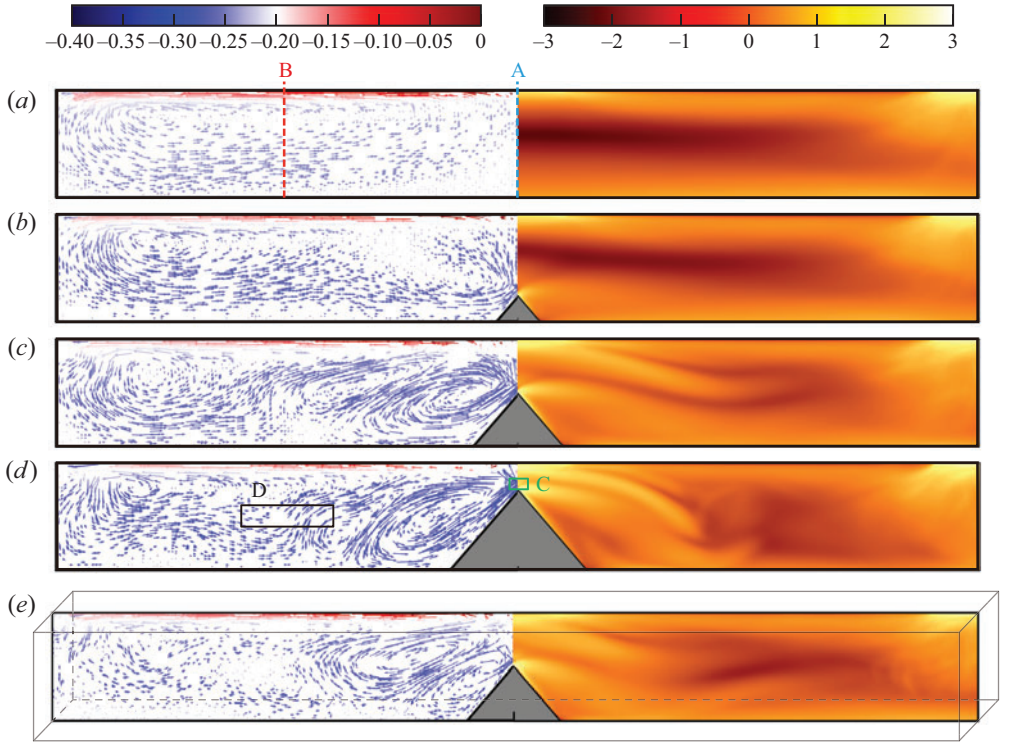

Figure 3. Temporally averaged velocity vectors (left half) and viscous dissipation rate ϵ_v in log scale (right half) corresponding to $h/H = 0$, 0.25, 0.5 and 0.75 from (*a*) to (*d*) for $\omega = 0.04$. (*e*) The cross-section at $y = W/2$ for the three-dimensional case with $h/H = 0.5$ and $\omega = 0.04$. The velocity vectors are coloured according to the local temperature θ. The length of the vectors are proportional to the velocity magnitude. The dashed lines labelled A and B indicate the position of the topography $x/L = 1$ and the bulk regions $x/L = 0.5$, respectively. The rectangles C and D in panel (*d*) respectively denote the region ($x \in [0.98, 1.02]$, $y \in [0.15, 0.17]$) and ($x \in [0.4, 0.6]$, $y \in [0.08, 0.12]$).

To examine the global influence of tide and topography, we present the volume-integrated dissipation $\mathcal{E}$ in figure 4. As shown in the figure, for the cases with large frequencies ($\omega \gtrsim 0.4$), results for different topography heights collapse together and approach the value for the case where both topography and tidal force are absent. Because the tidal velocity $U_{tide} = A/\omega$ is inversely proportional to the frequency ω, for large enough ω, the tidal velocity can be negligibly small compared with the background flow driven by buoyancy. Thus, for high tidal frequency, the system is governed by buoyancy. This explains why the dissipation strength is similar to the no-tide case. It also implies that when the tidal effect is weak or absent, topography alone has a negligible effect on the global dissipation. When ω reduces to approximately 0.1, enhancement in global viscous dissipation can be observed. Such enhancement enlarges when ω is further decreased (U_{tide} increases). Moreover, we observe that for larger h/H, the enhancement is stronger, which is consistent with the field observation that higher topography induces stronger local dissipation (Waterhouse *et al.* 2014). This result can be explained by the strong flow at the area adjacent to the topography, which significantly enhances the local dissipation, as shown in figure 3. The flow strength increases as h/H increases, so a higher topography induces a stronger enhancement in ϵ_v near the topography, and yields larger global dissipation for ω larger than a certain value (figure 4). However, figure 4 also

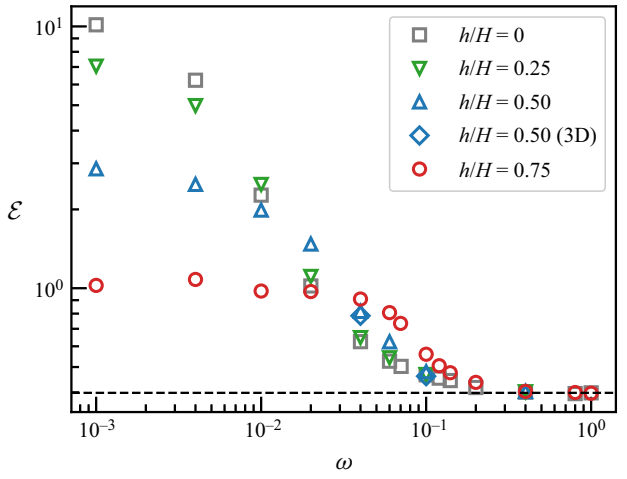

Figure 4. Volume-integrated viscous dissipation. The dashed line indicates the dissipation in the absence of tidal force and topography.

shows that there exists a crossover and gradual saturation in the global dissipation, i.e. for a particular topography of a given height, there seems to exist a certain h-dependent frequency below which the total dissipation starts to saturate and becomes smaller than the dissipations for topographies with smaller height. This may be understood in the following way.

The acceleration of fluid induced by tidal force is horizontal. Thus, when the topography becomes sufficiently high, it may also act as a blockage that hinders the acceleration of the fluid. As a result, viscous dissipation for higher topography can be smaller. This can also explain the result where the cases with a higher topography enter the saturated state at a higher ω (smaller U_{tide}), because the blockage effect is stronger for a higher topography. For $h/H = 0$, the global dissipation $\mathcal{E}$ also exhibits a trend that it asymptotically approaches a constant value at small ω (i.e. $\omega \leqslant 10^{-3}$). Unlike the tidal force that has a constant amplitude, the viscous drag between the fluid and the boundaries increases as ω decreases. Thus, at a certain ω, the viscous drag can become comparable to the tidal force and the former becomes the limiting factor for fluid acceleration. This suggests that the saturated state of the viscous dissipation can be understood as a balance between the tidal force and the combination of both the blockage effect of the topography and the boundary viscous drag. Such blockage and drag effects become important to the system when ω is small or equivalently U_{tide} is large. As ω further decreases (and equivalently U_{tide} increases), the blockage and drag effects increase and gradually become significant. As a result, the enhancement of $\mathcal{E}$ becomes less sensitive to ω and it asymptotically approaches a saturated state independent of ω.

4.2. *Tidal power*

As discussed in the previous section, the strength of the tidal force determines the change of global viscous dissipation. In this section, we separate the tidal power from the total viscous dissipation. As shown in figure 4, the influence of topography changes as ω varies. Because we fix the amplitude of the tidal force A in our study, decreasing ω is equivalent to increasing the tidal velocity U_{tide}. If the fluid moves along with the tide

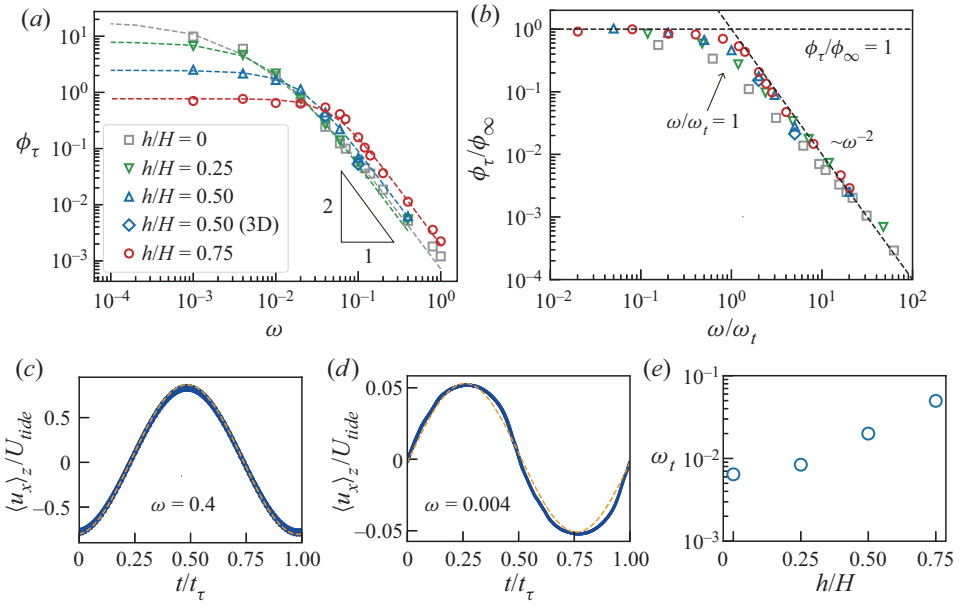

Figure 5. (*a*) Tidal power ϕ_τ as a function of ω for different topographies. The dashed lines represent the fitting of (4.2) to the data points. (*b*) Normalized tidal power ϕ_τ/ϕ_∞ as a function of ω/ω_t. The horizontal dashed line refers to $\phi_\tau/\phi_\infty = 1$ and the inclined dashed line refers to $\phi_\tau/\phi_\infty = (\omega/\omega_t)^{-2}$. The blue curves in panels (*c*,*d*) correspond to the normalized mean horizontal velocity $\langle u_x\rangle_z/U_{tide}$ at location B as a function of t/t_τ for $\omega = 0.4$ and 0.004, respectively. Here, $t_\tau = 2\pi/\omega$ is the tidal period. The dash curves are the best-fit sinusoidal function of the data points. Its amplitude is fixed to be $\max(\langle u_x\rangle_z)/U_{tide}$. Normalized topography height h/H equals to 0.75 for both panels (*c*,*d*). Transitional frequency ω_t as a function of h/H is shown in panel (*e*).

without obstruction, the work done by tidal force should follow the scaling relation $\phi_\tau \sim AD \sim \omega^{-2}$, where D is the tidal excursion $D = A\omega^{-2}$. The fluid velocity could be different from U_{tide}, owing to the existence of viscous drag between the fluid and the boundaries and blockage effect of the topography. For this reason, the efficiency of the tidal force in driving the flow with respect to different topographies is crucial for understanding the behaviour of $\mathcal{E}$, as shown in figure 4. To study the influence of the tidal force alone on the global energy balance, we separate ϕ_τ from $\mathcal{E}$ according to (3.3). Figure 5(*a*) shows the tidal power ϕ_τ as a function of ω, in which two distinguishable scaling relations between ω and ϕ_τ can be observed. For large ω, it follows a power law relation $\phi_\tau \sim \omega^{-2}$. This result suggests that the fluid motion is governed by the tidal force, so that ϕ_τ follows a linear relation with the tidal excursion D. This picture is further supported by the results of normalized horizontal mass flux $\langle u_x\rangle_z/U_{tide}$ shown in figure 5(*c*). From the figure, we observe that $\langle u_x\rangle_z/U_{tide}$ perfectly agrees with the sinusoidal function indicated by the orange dashed curve, which shows that the horizontal net flux is determined by the tidal force. Moreover, cases with a higher topography yield larger ϕ_τ in this regime, which can be understood as a result of the enhancement induced by the tide–topography interaction.

As ω further decreases, the system reaches another regime where ϕ_τ asymptotically approaches to a constant ϕ_∞ and becomes independent of ω. In this regime, the flow can no longer accelerate as the tidal excursion D increases. As shown in figure 5(*d*), the mean horizontal velocity deviates from the sinusoidal function. Considering that the viscous drag between fluid and boundaries scales with flow strength, this regime can

be explained as a result of the balance between the tidal force and the viscous drag. As the flow velocity increases, the velocity gradient near boundaries increases, which also strengthens the shearing effect. The tidal velocity U_{tide} increases as ω decreases, so viscous drag increases as well. When viscous drag becomes sufficiently strong to balance the tidal force, the flow can not further accelerate. As a result, the kinetic energy of the system reaches its bottleneck and becomes constant. For higher topography, this constant ϕ_∞ is smaller, which is consistent with the results for $\mathcal{E}$ in figure 4. Also, for different topography, the transition frequency from the perfect responsive state ($\phi_\tau \sim \omega^{-2}$) to the balance state ($\phi_\tau \approx \phi_\infty$) is different. In figure 5(*a*), it can be observed that for smaller h/H, the transition is less steep and occurs at a smaller ω. To discuss the transition of ϕ_τ quantitatively, we need a consistent method to extract the transition frequency.

We define the transition frequency ω_t as the intersection of two scaling relations $\phi_\tau \sim \omega^{-2}$ and $\phi_\tau = \phi_\infty$. A usual method to obtain ω_t is by fitting data governed by these two relations and taking the intersection. However, such a method is not realistic to use in this system, especially for small h/H. We notice that for small h/H, the transition is gradual. It requires extremely low frequency for the system to fully reach the saturated state with ω-independent tidal power $\phi_\tau = \phi_\infty$. For low frequency, however, the tidal period is very long. Take $\omega = 1 \times 10^{-3}$ as an example, where each tidal period equals up to 6283 free-fall time units. To ensure the system is statistically convergent, simulations for at least several times of the tidal period are required. Thus, it is computationally expensive to explore such an extremely small frequency regime for all geometries. Under the constraint of keeping reasonable computational cost, we use an alternative method to extract ω_t as well as ϕ_∞. We define the following transitional function:

$$\phi_\tau = \frac{\phi_\infty}{1 + B\omega + \dfrac{\omega^2}{\omega_t^2}}, \tag{4.2}$$

where ϕ_∞, B and ω_t are parameters to be determined. Such a function approaches $\phi_\tau = \phi_\infty \omega_t^2/\omega^2$ when $\omega \gg \omega_t$. As for $\omega \ll \omega_t$, it asymptotically converges to $\phi_\tau = \phi_\infty$. The intersection of these two asymptotic lines is $\omega = \omega_t$. Because the first-order term ω^1 decreases slower than the second-order term ω^2 as ω decreases, the term $B\omega$ helps to tune the steepness of the transition. The fitting results of (4.2) are given by the dashed curves in figure 5(*a*). It shows that ϕ_τ can be described properly by (4.2). The normalized tidal power ϕ_τ/ϕ_∞ as a function of ω/ω_t is shown in figure 5(*b*). Despite the discrepancy at $\omega \approx \omega_t$ caused by the difference in transition steepness between the different cases, the results of different h/H collapse well. The larger h/H topographies produce a stronger obstacle effect. Thus, as shown in figure 5(*e*), the transition frequency ω_t is larger for higher topography, which is equivalent to a smaller transitional tidal velocity U_{tide}^t. As a result, higher topography yields a smaller saturation constant ϕ_∞, as shown in figure 5(*a*).

We briefly summarize the findings from the results of tidal power shown in figure 5. Higher topography can benefit the tidal power through a stronger tide–topography interaction, but it may also obstruct further acceleration of the flow and induce a smaller degree of global viscous dissipation. A determinant ingredient is the strength of viscous drag, which increases along with U_{tide}. According to the strength of the viscous drag, two distinguished regimes of tidal power can be separated, as observed in figure 5. For $\omega/\omega_t > 1$, the tidal power is proportional to the tidal excursion, which yields $\phi_\tau \sim \omega^{-2}$, consistent with the picture that the flow is governed by the tide. However, for $\omega/\omega_t < 1$, as viscous drag increases, ϕ_τ becomes less sensitive to ω, and asymptotically approaches

a constant ϕ_∞. Such a regime is the result of balancing between viscous drag and tidal force, so the strength of the viscous drag determines the upper limit of the tidal power. By comparing figures 4 and 5(*a*), we find that in this regime, ϕ_τ contributes the vast majority of $\mathcal{E}$, i.e. $\mathcal{E} \sim \phi_\tau$. Thus, ϕ_τ behaves similarly as $\mathcal{E}$ for small ω. This implies that not only the tidal power but also the global dissipation is bounded by viscous drag. For this reason, we conclude that $\omega < \omega_t$ corresponds to the regime of drag-control in this system. As for $\omega > \omega_t$, though ϕ_τ is controlled by the tide, by comparing figures 4 and 5(*a*), we see that the behaviours of ϕ_τ and $\mathcal{E}$ are different. This means that a more detailed regime separation is needed for $\omega > \omega_t$.

4.3. *Reynolds number*

In the previous section, we have identified a regime corresponding to drag control. In this regime, tidal force is balanced by viscous drag, and the latter determines the upper limit of ϕ_τ as well as $\mathcal{E}$. Other than the tidal force, buoyancy is another energy source that maintains the fluid motion of this system. For a classical HC system, buoyancy is the only energy source of this system. When a tidal force is introduced, the competition between the tidal force and buoyancy determines the global dissipation. To quantitatively compare the respective contributions of tidal force and buoyancy to the flow, we discuss the features of velocity components corresponding to these two mechanisms. In an HC system, the fluctuation of velocity induced by buoyancy mainly arises from plume detachments from the cold plate. Because these plumes will be soon dissipated after detachment, at locations such as B shown in figure 3, i.e. in the bulk and away from cold plate, the fluctuation of u_x is not induced by buoyancy but caused by the tidal force. Thus, at these locations, the fluctuation caused by the tidal force will be averaged out if time averaging is used. The remaining non-periodic component is related to the buoyancy driving. For this reason, the time-averaged background velocity $u_{bg} = \langle u_x \rangle_t$ can represent the flow strength of the background flow that is mainly induced by buoyancy driving. However, the velocity fluctuation $u_{rms} = \sqrt{\langle u_x^2 \rangle_t - u_{bg}^2}$ reflects the strength of tidal flow. The third one is the mean squared velocity $u_{tot} = \sqrt{\langle u_x^2 \rangle_t}$ representing the combined effect of buoyancy and tidal drivings to the flow. The contributions of different mechanisms can be measured according to the magnitudes of different components of u_x. We define U_{bg} as the average from $x/L = 0.5$ to $x/L = 1.5$ of the vertical maxima of u_{bg}. Here, U_{rms} and U_{tot} are evaluated by u_{rms} and u_{tot} accordingly. Corresponding to the above three velocities, three Reynolds numbers are defined: (1) Re_{bg} using mean velocity U_{bg}, which represents the flow strength driven by buoyancy; (2) Re_{rms} using the r.m.s. velocity U_{rms}, which represents the flow strength driven by the tidal force; and (3) Re_{tot} using the mean squared velocity U_{tot}, which represents the collective effect of the two driving forces.

Results for Re_{bg}, Re_{rms} and Re_{tot} are shown in figure 6(*a–c*), respectively. The inclined grey dashed lines shown in all three plots represent $Re_{tide} \equiv Re_{tide}(\omega) = \sqrt{Ra/Pr}A/\omega$, which is the Reynolds number evaluated using the tidal velocity. Figure 6(*a*) shows the results for Re_{bg}, which represents the background flow strength driven by buoyancy. We can see from figure 6(*a*) that for large ω, Re_{bg} is much larger than Re_{tide}. This implies that the system is dominated by the background flow that is driven by buoyancy. Also, Re_{bg} is nearly constant for all values of h/H, which suggests that the dominant background flow structure is similar to the case in the absence of a tidal force, which is the large-scale circulation. For large ω, such a background flow is largely unaffected by the tidal force.

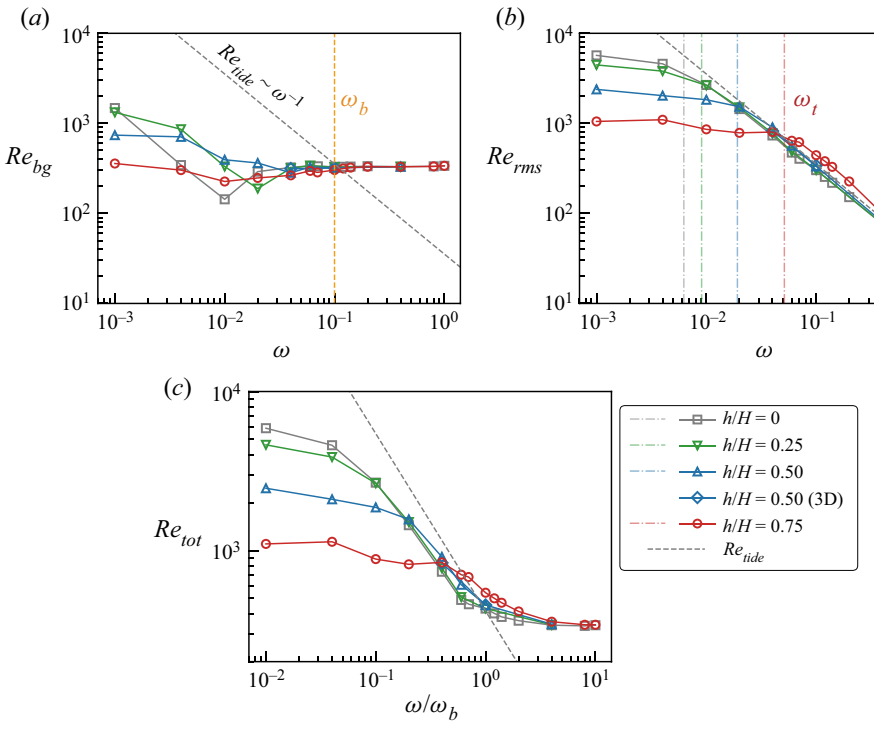

Figure 6. Reynolds numbers: (*a*) Re_{bg} is evaluated using U_{bg}; (*b*) Re_{rms} using U_{rms} and (*c*) Re_{tot} using U_{tot}. The grey dashed lines represent $Re = Re_{tide}(\omega)$. In panel (*a*), the vertical orange dashed line corresponds to ω_b. Vertical dash–dotted lines shown in panel (*b*) denote ω_t.

As ω decreases, a crossing between Re_{bg} and Re_{tide} is observed. This crossing frequency ω_b is denoted by the orange vertical dashed line in figure 6(*a*). Because both Re_{tide} and Re_{bg} are independent of h/H, ω_b is the same for all topographies. For $\omega < \omega_b$, Re_{tide} becomes much larger than Re_{bg}, which shows that the system is now dominated by the tidal flow. Moreover, Re_{bg} becomes sensitive to both ω and h/H. This also suggests that the tidal force is dominant so that it can reconstruct the mean flow structure, as demonstrated in figure 3. By comparing Re_{tide} and Re_{bg}, we find a topography-independent transitional frequency ω_b that separates the buoyancy-control and tide-control regimes. In addition to the drag-control regime with $\omega < \omega_t$, three distinguished regimes can be detected in this system.

In figure 6(*b*), the vertical dash–dotted lines denote the transition frequency to the viscous control regime ω_t. Results of Re_{rms} behave almost similarly as ϕ_τ shown in figure 5(*b*). Similar to the results of ϕ_τ, it is clear to see that ω_t separates two different regimes in Re_{rms}. For $\omega > \omega_t$, Re_{rms} is approximately equal to Re_{tide}, which indicates that the horizontal fluctuating motions are governed by the tidal force. For $h/H = 0.75$, the magnitude of Re_{rms} is larger than the others, which is attributed to the stronger tide–topography interaction. In this parameter range, the increase of the viscous drag as the tidal velocity U_{tide} increases is negligible. Thus, the fluctuation of the flow is strengthened correspondingly. For $\omega < \omega_t$, the viscous drag becomes comparable to the tidal force, then the system enters the drag-control regime. In this case, Re_{rms} becomes less sensitive to ω and asymptotically approaches a constant.

The results of Re_{tot}, shown in figure 6(c), represent the combined effect of the tide and buoyancy forces on the global flow strength. These results have basically similar behaviour as the global viscous dissipation shown in figure 4. In the buoyancy-control regime ($\omega > \omega_b$), the tidal effect is insignificant, so that the buoyancy works as the governing mechanism. For this reason, Re_{tot} is not sensitive to ω. As ω decreases and approaches to ω_b, the system enters the tide-control regime. The magnitude of Re_{tot} is consistent with Re_{tide}, which shows that the tidal force governs the flow of this system. When the system enters the drag-control regime $\omega < \omega_t$, Re_{tot} deviates from Re_{tide} and becomes less sensitive to ω, as a result of the balancing between viscous drag and tidal force. Similar to the global dissipation shown in figure 4, higher topography yields smaller Re_{tot} at this saturated state.

The quantity ϕ_i is always positive in the system. Thus, although the temperature distribution underneath the cold plate is thermally unstable, the overall system is stably stratified. For a stratified system, the turbulence level can be characterized by the buoyancy Reynolds number Re_{buo} (Smyth & Moum 2000; Salehipour & Peltier 2015; Monismith, Koseff & White 2018), which is defined as

$$Re_{buo} \equiv \frac{\epsilon_v^d}{\nu N^2}, \tag{4.3}$$

where $\epsilon_v^d \equiv \nu \sum_i \sum_j (\partial u_i^d / \partial x_j^d)^2$ is the dimensional viscous dissipation, and u^d and x^d are the dimensional velocity and coordinate, respectively. Using the non-dimensionalizing reference parameters and (3.3), the mean buoyancy Reynolds number of the system can be written as

$$Re_{buo} = \frac{1}{Pr}\frac{\langle \mathcal{E} \rangle_t}{\langle \phi_i \rangle_t} = \frac{1}{Pr} + \frac{1}{Pr}\frac{\langle \phi_\tau \rangle_t}{\langle \phi_i \rangle_t}. \tag{4.4}$$

The first term $1/Pr$ on the right-hand side of (4.4) is attributed to the surface buoyancy flux (i.e. the HC contribution), which is always a constant $1/Pr$ independent of Ra. We show the results of Re_{buo} in figure 7(a), for the buoyancy-control regime ($\omega < \omega_b = 0.1$), the magnitudes of Re_{buo} are close to $1/Pr$ and almost independent of ω. This implies that for any practical Prandtl numbers of the ocean, the surface thermal forcing itself can not sustain a system with spontaneous turbulence generation in the interior, no matter how high the Rayleigh number is. Even though the region underneath the cold plate can be significantly turbulent owing to plume emissions, one expects that the flow would become laminar once these turbulent structures are dissipated. In other words, the turbulent structures observed in horizontal convection at high Rayleigh numbers are most likely undissipated plumes. From (4.4), one also sees that $Re_{buo} \to \infty$ as $Pr \to 0$. This suggests that horizontal convection is theoretically able to generate intense turbulence at low Pr, if one is allowed to go beyond the parameter range of the real ocean.

The second term in (4.4) refers to the mechanical energy contribution. Similar to the global dissipation $\mathcal{E}$ shown in figure 4, Re_{buo} increases as ω decreases once the system becomes tide controlled, and becomes saturated when it enters the drag-control regime. This result suggests that ϕ_i is much less sensitive to ω than ϕ_τ. Rewriting (4.4) gives $Re_{buo} - 1/Pr = \langle \phi_\tau \rangle_t / (Pr \langle \phi_i \rangle_t)$. We present the results of $Re_{buo} - 1/Pr$ in figure 7(b). We observe that $Re_{buo} - 1/Pr \sim \omega^{-2} \sim Re_{tide}^2$ in both the tide- and buoyancy-control regimes, which is similar to the results of ϕ_τ shown in figure 5. Figure 7(a) also shows that the buoyancy Reynolds number is small in the current study ($Re_{buo} < 10$), which indicates the low turbulence intensity in the current parameter range. We also note that the magnitude of Re_{buo} is smaller than most of those observed in the open ocean ($Re_{buo} \lesssim 100$,

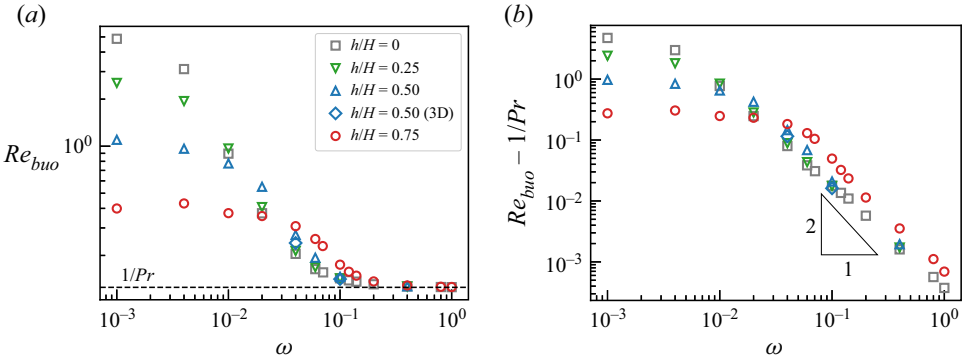

Figure 7. (*a*) Buoyancy Reynolds number Re_{buo} and (*b*) $Re_{buo} - 1/Pr$ as a function of ω. The horizontal dashed line represents $Re_{buo} = 1/Pr$.

see Monismith *et al.* 2018). This again shows that the local mixing mechanism in the current study could be different from that in the ocean, and we should instead focus on the global quantities and energy budgets. From this perspective, (4.4) shows that the tide (or other mechanical sources) is much more important than the surface buoyancy flux in the maintenance of turbulence intensity in the ocean interior.

4.4. *Nusselt number*

Heat transfer is one of the global transport quantities that respond to driving forces. We plot Nu as a function of ω in figure 8. For sufficiently large ω, cases with different h/H yield the same constant Nu that is independent of ω, which suggests that the global heat transfer is governed by the buoyancy and not affected by the tidal force. However, Nu starts to increase when ω becomes smaller than a certain frequency. Figure 8(*b*) shows clearly that this certain frequency is ω_b, which provides further evidence that ω_b is the transition frequency separating the buoyancy- and tide-control regimes. For $\omega < \omega_b$, significant Nu enhancement can be observed. From figure 8, we see that in both the tide- and drag-control regimes, Nu is obviously larger than in the buoyancy-control regime. The largest Nu enhancement observed in this study reached 1.6 times the case without tide, as shown in figure 8(*b*). The behaviour of Nu as a function of ω at the tide- and drag-control regimes is complicated, especially for high topography. Unlike global viscous dissipation where higher topography yields larger $\mathcal{E}$ in tide-control regime, the enhancement in Nu for high topography is insignificant. As for the drag-control regime, both topographies with $h/H = 0.5$ and $h/H = 0.75$ yield Nu smaller than the cases with a lower topography, which can be understood as a result of the weaker flow strength, as indicated by figure 6. Also, though Nu globally becomes less sensitive to ω, we observed that locally, Nu is non-monotonic as ω decreases for $h/H = 0.5$ and 0.75. This result could be related to the changes of flow structure. As illustrated by the vector field shown in figure 3(*c*,*d*), large vortex structures can be observed near topography. Large-scale circulation is significantly altered by the vortex structures. As ω decreases, such vortex structures evolve as well. Thus, complex behaviour in Nu can be observed for $h/H = 0.5$ and $h/H = 0.75$ when ω is small. Moreover, an interesting finding can be observed where for $h/H = 0.25$, the amount of Nu is larger than the case in the absence of topography. This result could be understood as follows. For $h/H = 0.25$, the topography is not high enough to induce any sizeable vortex structures to disrupt the horizontal heat transfer pathway, as demonstrated

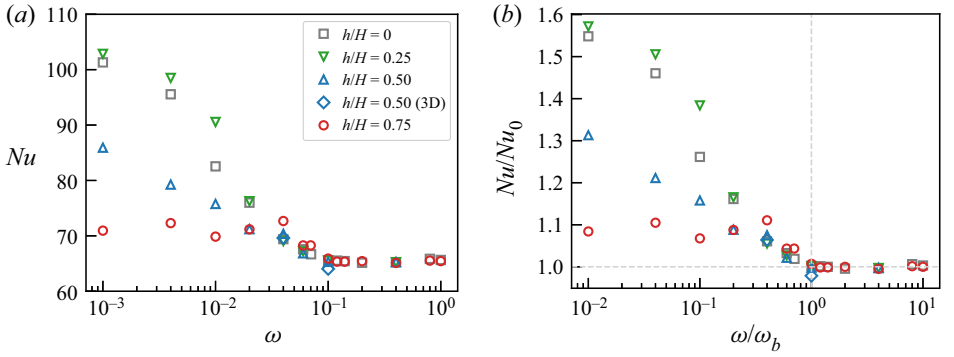

Figure 8. (*a*) Nusselt number Nu as a function of ω for different topographies, and (b) the normalized Nusselt number Nu/Nu_0 as a function of ω/ω_b. Here, Nu_0 corresponds to Nu obtained in the case without tide and topography.

in figure 3(*b*). However, the tide–topography interaction can directly enhance the flow strength near the hot plate, which results in a stronger shear at the plate and a thinner thermal boundary layer. Thus, the Nu for $h/H = 0.25$ is larger than that for the smooth case.

Additional evidence for the transition from the buoyancy- to tide-control regimes can be found from the time series of Nu. In figure 9, we plot the time series of Nu_{hot} and Nu_{cold} as a function of t/t_τ for different ω/ω_b. Here, Nu_{hot} and Nu_{cold} are Nusselt numbers evaluated according to the temperature gradient at the hot and cold plates, respectively. Figure 9(*a–d*) is for $h/H = 0.75$ and figure 9(*e–f*) is for $h/H = 0$, and in the plot, time t is normalized by the tidal period $t_\tau = 2\pi/\omega$. It is seen that in the buoyancy-control regime, i.e. $\omega/\omega_b > 1$ (figure 9*a*,*b*,*e*,*f*), Nu_{cold} fluctuates strongly and Nu_{hot} is relatively steady. Such a result agrees with the picture of a classical HC system, which can be understood as downwelling plumes from the cold plate inducing fluctuations in Nu_{cold}. Because the hot plate is thermally stable, no plume detachments are observed. Thus, conduction is the main form of heat transfer at the hot plate, which makes Nu_{hot} fluctuate with a much smaller amplitude than Nu_{cold}. When ω/ω_b approaches 1, a nearly periodic variation with period equal to $0.5t_\tau$ can be observed in the time series for both Nu_{hot} and Nu_{cold}, as shown in figure 9(*c*,*g*). Such periodicity in Nu indicates that the tidal force is already strong enough to affect the thermal boundaries at the hot and cold plates. Moreover, from the time series of Nu_{cold} shown in panels (*c*,*g*), we observe that the local fluctuation related to plume detachment is smaller than the amplitude of the periodic signal related to the tidal force, i.e. the modulation amplitude is larger than the high frequency fluctuations. This result implies that tidal force overtakes buoyancy and controls global heat transfer. The periodicity of the Nu time series continues for $\omega/\omega_b < 1$, as shown in panels (*d*,*h*). Unlike the cases for $\omega/\omega_b \geqslant 1$, where Nu_{cold} exhibits more fluctuation than Nu_{hot}, we observe that the amplitudes of Nu_{hot} and Nu_{cold} are almost similar, which shows that the tidal shearing dominates the global heat transfer and convection becomes less important.

4.5. *Viscous dissipation profiles*

To examine the influence of the different controlling mechanisms to local dissipation, we compare the vertical profiles of the local energy dissipation rate ϵ_v for different height h/H

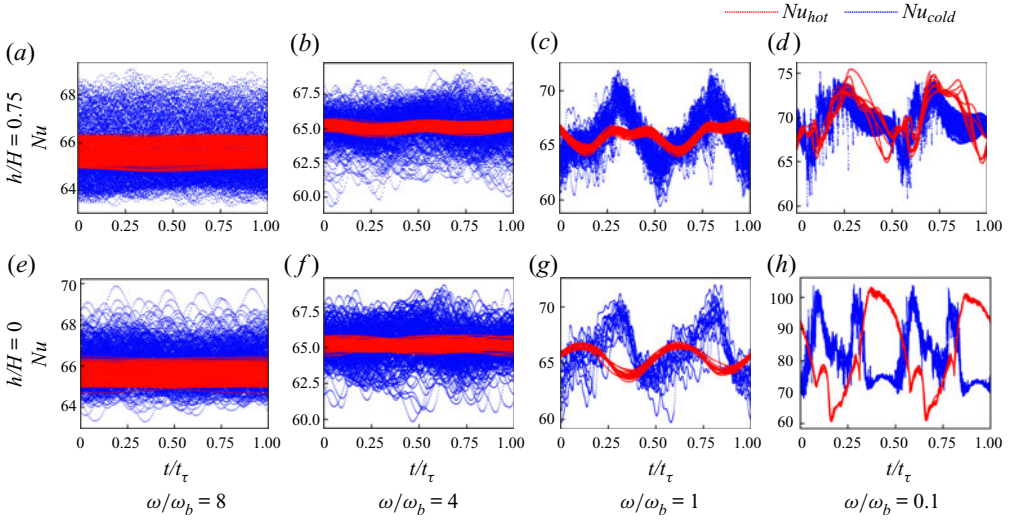

Figure 9. Time series of Nu_{cold} (blue dots) and Nu_{hot} (red dots) as a function of t/t_τ for different ω/ω_b. Panels (*a–d*) are for $h/H = 0.75$ and panels (*e–h*) are for a smooth bottom. Here, $t_\tau = 2\pi/\omega$ is the period of the tide.

of topography and tidal frequency ω. First, we present in figure 10 the profiles of different h/H in the same plot. The profiles are taken at two representative locations, as indicated by the vertical dashed lines A and B in figure 3(*a*). The columns from left to right correspond to no-tide, tidal frequency $\omega = 0.4$, 0.06, and 0.001, respectively.

Figure 10(*a–d*) corresponds to location A, which is in the position directly above the topography at $x = 1$, and each profile starts from the tip of the respective topography and ends at the top surface ($z/H = 1$). Heights of the topography are indicated by the respective horizontal dashed lines. The profiles above the topography for the no-tide cases are shown in figure 10(*a*). It can be observed that the dissipation profiles close to the top boundary are almost identical. Away from the top surface, the profiles for different topography heights are distinct from each other, because the topography lifts the bottom boundary layer and gives rise to different flow structures. However, their magnitudes are generally close to each other, which shows that the influence of the topography on the local flow is limited when there is no tide. Once a tidal force is introduced, as shown in panel (*b*), the shapes of the ϵ_v profiles are obviously changed. By comparing the profiles in panel (*b*), we observe that for higher topography, the magnitude of the entire profile of ϵ_v is larger than the cases with smaller h/H, which is consistent with the field observation where a higher topography induces stronger local dissipation (Waterhouse *et al.* 2014). When ω decreases to 0.06, as shown in panel (*c*), dissipation for all heights are clearly enhanced compared with the cases with a higher frequency, especially near the tip of the topographies. Like the previous cases for higher ω, a higher topography still yields stronger dissipation. However, as ω further decreases to 0.001, a higher topography no longer yields a larger dissipation than the cases with a smaller h/H, as shown in panel (*d*). Profiles of different h/H intersect and the magnitudes of them are close to each other. Such a result indicates that the sensitivity of the local dissipation enhancement to the change of ω depends on both the frequency and height of the topography. For high topography and small frequency, dissipation is less sensitive to the change of ω. Thus, the difference in ϵ_v

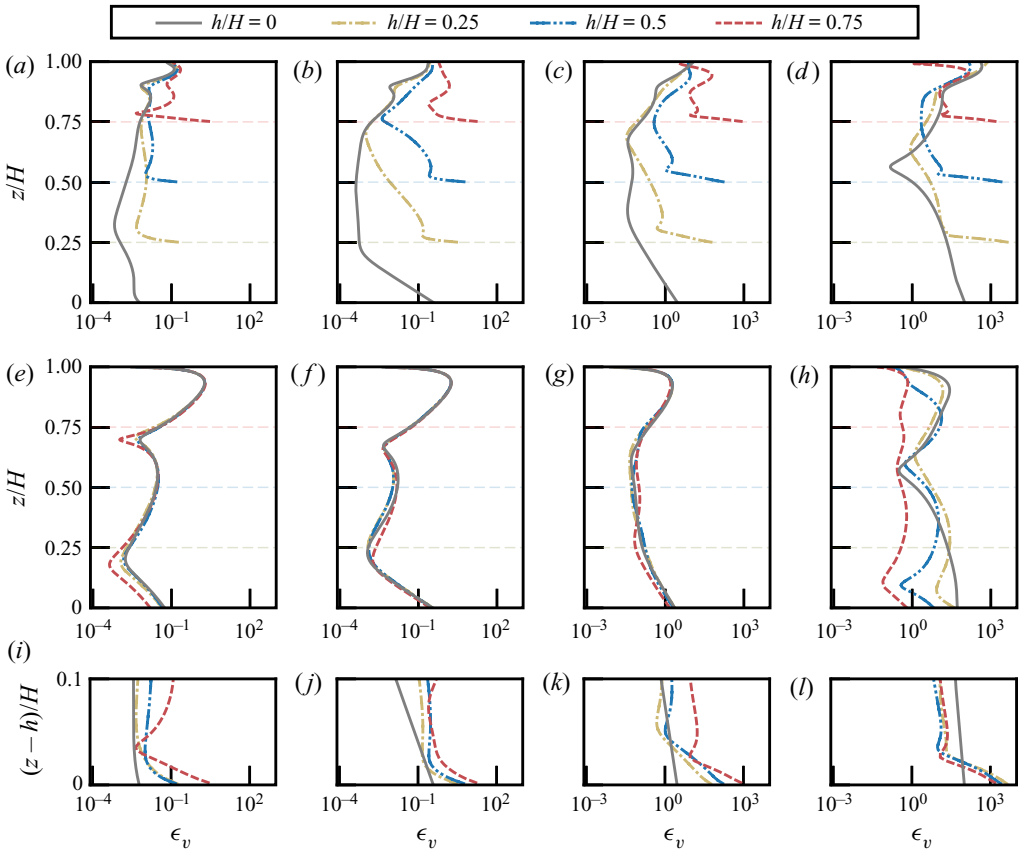

Figure 10. Profiles of viscous dissipation with different h/H in the same plot. (*a–d*) Profiles at location A, (*e–h*) profiles at location B and (*i–l*) the same profiles as in panels (*a–d*) but starting from the tip of the topography. The columns from left to right correspond to no tide, $\omega = 0.4$, 0.06 and 0.001, respectively.

between different h/H gradually becomes smaller and eventually results in the profiles we observe in figure 10(*d*).

Figure 10(*e–f*) corresponds to location B, which is in the bulk region ($x/L = 1/2$). For the situation without a tidal force, as shown in panel (*e*), the profiles of different topography collapse together and are almost identical. This result is not surprising, because the topography may modify flow structures at its surrounding area, but the region away from it should be unaffected. For $\omega = 0.4$, the system is still governed by the buoyancy force. Thus, the dissipation profiles shown in panel (*f*) are similar to the no-tide cases in panel (*e*). When ω decreases to 0.06 and becomes less than ω_b, the system has entered the tide-control regime. In this case, the profiles of different h/H still collapse together, as shown in panel (*g*). However, both the shape and the magnitude of these profiles are obviously distinct from those in panels (*e*,*f*), which indicates that the tidal force starts to affect the bulk flow, but the blockage and drag effect of the topography is still negligible. When ω is further decreased down to 0.001, significant deviation among profiles for different topographies can be observed, as shown in panel (*h*). The reason of this deviation is that the system has already entered the drag-control regime and the blockage and drag effect has become significant for the higher topography. For $h/H = 0.75$, the blockage

and drag effect are most significant among these cases. Thus, dissipation for $h/H = 0.75$ yields a minimum magnitude among the different cases in the bulk, even smaller than the case without topography.

By comparing the local dissipation profiles above the topography (*a–d*) and in the bulk (*e–h*), we can see the different influences of the topography in these two regions. For the region near the topography, dissipation is sensitive to the change of tide. Even for the buoyancy-control regime, as shown in panel (*b*), the dissipation profiles of different topographies differ from each other in magnitude. For the bulk region, however, not only for the buoyancy-control but also the tide-control regime, the dissipation profiles for different topographies can still collapse together, as shown in panels (*e–g*). This result indicates that the enhancement of dissipation induced by the tidal force is sensitive to h/H at the region near topography, but insensitive to h/H in the bulk. Moreover, by comparing the dissipation profile of $h/H = 0.75$ in panel (*h*) with those of other topographies, it can be found that the blockage and drag effect of high topography can clearly suppress the bulk dissipation enhancement. As for the topography region, however, higher topography does not yield an obviously smaller amount of local dissipation than the lower one, as shown in panel (*d*). This suggests that the blockage and drag effect are more significant in the bulk.

We further examine the local dissipation structures near topography in detail. Figure 10(*i–l*) is the same profiles as in panels (*a–d*) but aligned to the tip of the topography for the convenience of comparison. In both figures 10(*j*) and 10(*l*), we observe that the dissipation profiles directly above the tip are almost identical between the different topographies. Such similarity can not be observed in the cases without a tidal force, as shown in panel (*i*). As for panel (*k*), the profiles of $h/H = 0.25$ and 0.5 almost collapse, but for $h/H = 0.75$ the profile obviously deviates from the others. These behaviours can be better understood in terms of the regimes with different control mechanisms. It can be found that all the cases in panel (*j*) and for $h/H = 0.25$ and $h/H = 0.5$ in panel (*k*) correspond to the tide-control regime, so that the shapes of the dissipation profiles near the boundary are similar. As for $h/H = 0.75$ in panel (*k*) and all cases in panel (*l*), the system enters the drag-control regime. Thus, for $h/H = 0.75$ in panel (*k*), the dissipation profile is different to the others, and for panel (*l*), where all cases are again in the same regime. Then the dissipation profiles right above tips collapse together.

As shown in figure 10, the influence of topography on local dissipation depends on the tidal frequency ω. To examine the influence of the frequency ω on local dissipation, we then fix h/H and plot profiles for different ω in the same graph, as shown in figure 11. The columns from left to right correspond to $h/H = 0$, 0.25, 0.5 and 0.75, respectively. Figure 11(*a–d*) shows the profiles taken at location A, corresponding to the region right above the topography; and figure 11(*e–h*) shows the profiles measured at the bulk location B. For a better comparison between results with different h/H, the vertical axes in panels (*a–d*) are normalized by the gap width between the tip of the topography and the top boundary.

For most of the cases in figure 11(*a–d*), ϵ_v above the topography is seen to be sensitive to the changes in ω. We take figure 11(*b*) as an example. The profile of $\omega = 0.4$ is obviously different from that of the no-tide case, even though their magnitudes are close to each other, broadly speaking. As ω decreases, the viscous dissipation is enhanced. A similar enhancement in dissipation as ω decreases can be observed in the cases with different topography, as shown in panels (*a*,*c*,*d*). We observed that the enhancement is more significant for the case with higher topography when $\omega \geqslant 0.06$. For $\omega \leqslant 0.06$, as the system gradually becomes drag controlled, the enhancement in dissipation becomes less

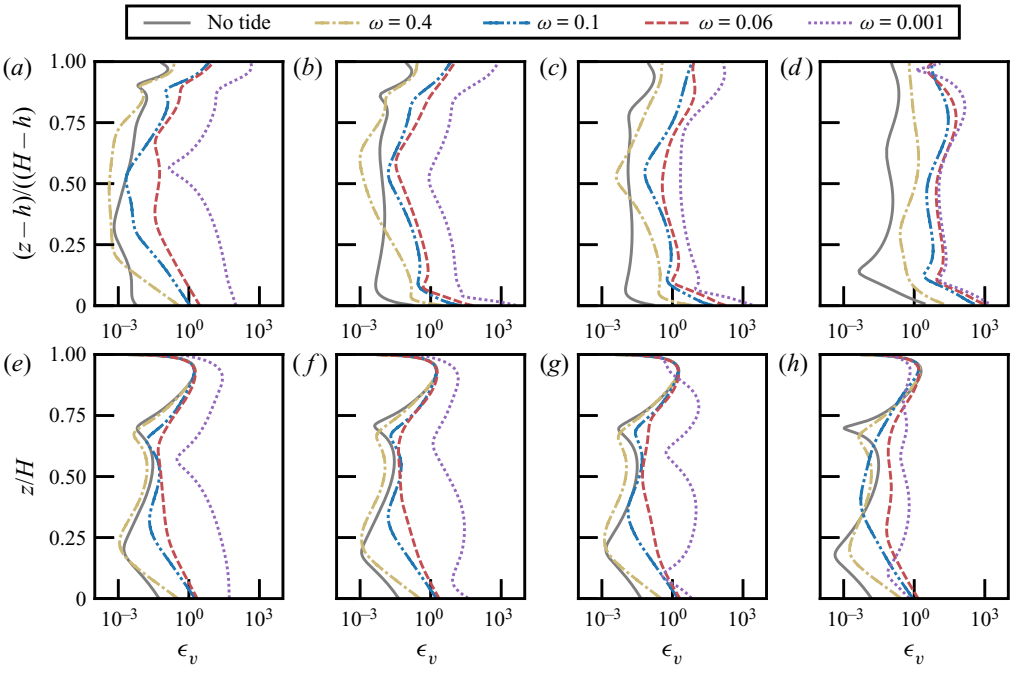

Figure 11. Profiles of viscous dissipation with different ω in the same plot. (*a–d*) Profiles measured at location A and (*e–h*) profiles measured at location B. Columns from left to right correspond to $h/H = 0$, 0.25, 0.5 and 0.75, respectively. Note that for panels (*a–d*), the vertical coordinate spans the gap between the tip of the respective topography and the top surface of the fluid body.

sensitive to the change of ω, especially for large topography height which has a stronger effect of blockage and drag on the flow. This result is most obvious in figure 11(*d*) with $h/H = 0.75$. It is clear that the profiles change very little from $\omega = 0.06$ to 0.001 in this case.

Enhancement of dissipation with decreasing ω can also be observed in the bulk region. Different from the region near the topography, where both shape and magnitude of the dissipation profiles change once the tidal force is introduced, the dissipation in the bulk is less sensitive to the tidal force. As shown in figure 11(*f*), for example, the result of $\omega = 0.4$ (corresponding to the buoyancy-control regime) has almost identical profile as the no-tide case. For $\omega > 0.4$, as the system gradually changes from buoyancy controlled to tide controlled, the bulk dissipation enhances as ω decreases. Similar results can also be observed in figure 11(*e*,*g*,*h*). Because for higher topography the transition frequency ω_t from the tide- to drag-control regime is larger, it can be observed that the enhancement of dissipation for larger h/H is smaller than the lower ones when $\omega \leqslant 0.06$. This difference is most obvious when comparing the profiles for $h/H = 0.75$ shown in panel (*h*) with those in panels (*e*,*f*). For $\omega = 0.06$ and 0.001 in panel (*h*), though the profiles of dissipation are different, their magnitudes are very close to each other, which suggests that the system enters the drag-control regime, in which drag force is comparable to the tidal force. These results show that the bulk dissipation can also be affected by topography when the tidal frequency is low. As ω decreases, the blockage effect of topography becomes increasingly significant, which leads to a reduced sensitivity of the dissipation enhancement on ω. For higher topography, the blockage effect is stronger and its onset starts at a large ω, and

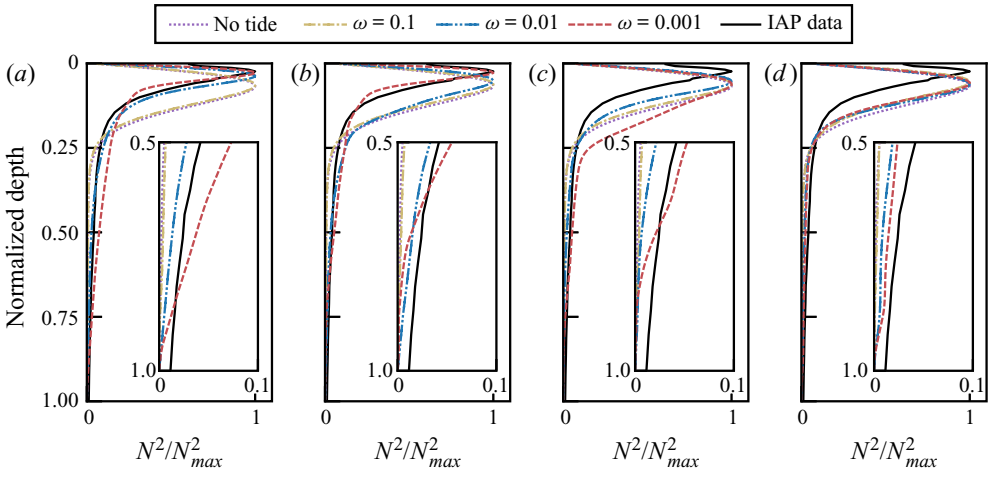

Figure 12. Profiles of normalized N^2 at location B shown in figure 3 for (*a*) $h/H = 0$, (*b*) 0.25, (*c*) 0.5 and (*d*) 0.75. The black solid curves refer to oceanic data (Li *et al.* 2020). The insets are zoom-in views for the region with normalized depth larger than 0.5.

eventually induces a smaller magnitude of dissipation in the bulk, as shown in figures 10 and 11.

4.6. *Stratification and flow patterns*

Abyssal stratification is another important feature in the system. In classical HC, the interior is well mixed and with relatively weak stratification in the abyss (Mullarney *et al.* 2004). Such weak stratification is not sufficient to sustain the abyssal internal waves, which are vital in the mixing of the ocean interior (Munk & Wunsch 1998). We show the buoyancy frequency profiles normalized by its maximum value as a function of normalized depth in figure 12 and compare them with the mean stratification profile of the ocean. Data for the ocean are collected from the IAP group (Li *et al.* 2020) and averaged spatially over 20°CN to 20°CS and temporally over 2010 to 2018. The normalized depth is defined as $(H - z)/H$ for simulations and d/H_{ocean} for the ocean, where d is depth and $H_{ocean} = 2000$ m. In the buoyancy-controlled regime ($\omega > 0.1$), it is true that the abyssal stratification observed in our study is much weaker than that of the ocean. However, when the system enters the tide-controlled regime ($\omega < 0.1$), we can find a stratification close to (e.g. $\omega = 0.01$ in figure 12*a*) or even more robust than the ocean ($\omega = 0.001$ in figure 12*a*). This result is surprising, because tidal force is usually considered as a trigger of abyssal internal waves but not a maintainer of stratification. This result reveals the importance of tidal force in maintaining abyssal stratification and suggests another possibility of the role of tidal force in the abyssal ocean.

As previously mentioned, we do not focus on the local structures of this system. Nevertheless, the flow structures for different tidal frequencies can qualitatively exhibit the features of the different regimes of this system. Thus, we present the velocity vectors for different ω in figure 13. We find that for the buoyancy-controlled regime, the downwelling flows induced by plume emissions are the most significant fluid motion in the system. As the tidal frequency decreases, one can observe an overall enhancement of the flow strength. When the system enters the tide-controlled regime, the downwelling flow underneath the cold plate is no longer dominant. The flow in the vicinity of topography becomes strong.

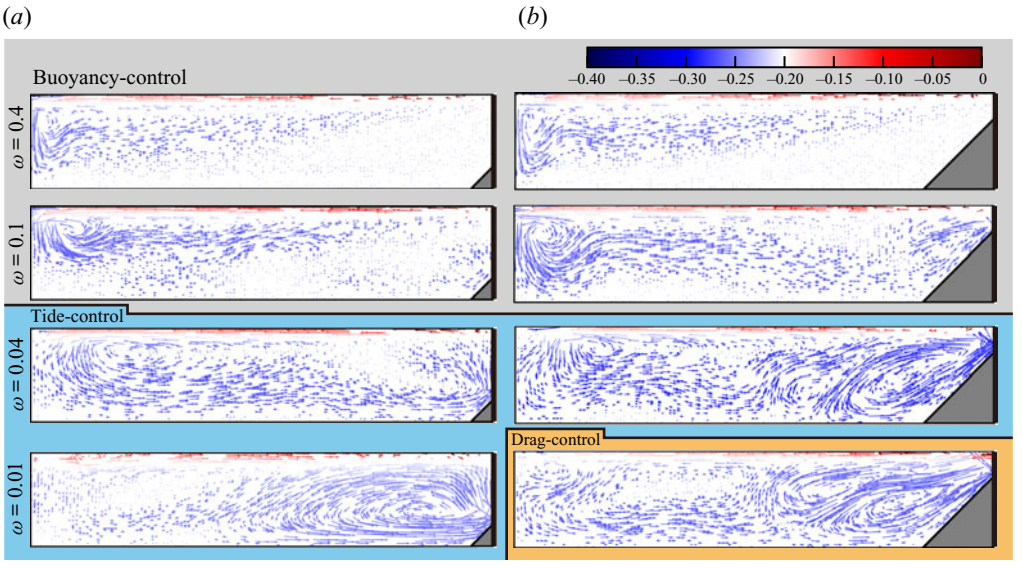

Figure 13. Temporally averaged velocity vectors for $h/H = 0.25$ (a) and $h/H = 0.75$ (b). The velocity vectors are coloured according to the local temperature θ. The length of the vectors are proportional to the velocity magnitude. Different shaded regions denote different flow regimes.

In some cases, these flows can be even stronger than those in the plume-emitting region (such as $\omega = 0.04$ for $h/H = 0.75$). The mean flow strength of the system keeps increasing as ω decreases until the system enters the drag-controlled regime. Comparing $\omega = 0.04$ (corresponding to the tide-controlled regime) and $\omega = 0.01$ (corresponding to the drag-controlled regime), one can see that either flow structure or flow strength in these two cases are very similar. Such a result suggests that the flow strength becomes independent on tidal frequency when the system enters the drag-controlled regime.

4.7. *Mixing efficiency*

In this section, we discuss the mixing efficiency η defined by (3.5). The dependence of η as a function of ω is shown in figure 14. For large ω, different topographies converge to the same value which is η_{HC}. This can be explained by the results discussed previously that both global dissipation $\mathcal{E}$ and $G(APE)$, indicated by Nu, are insensitive to either topography height or tidal frequency ω in the buoyancy-control regime. The constant η_{HC} ($\approxeq 0.85$) is much larger than the empirical value 0.2 used in most models for oceanic circulations. This high mixing efficiency is comparable with the results from other studies considering only buoyancy force (Scotti & White 2011; Sohail *et al.* 2018; Wang *et al.* 2018). A transition to the tide-control regime occurs when $\omega \approx \omega_b$, after which η decreases with ω. From (3.5), one can obtain

$$\frac{\partial \eta}{\partial G(APE)} = \frac{\mathcal{E}}{(\phi_d + \phi_\tau)^2}, \tag{4.5a}$$

$$\frac{\partial \eta}{\partial \phi_\tau} = -\frac{\phi_d - \phi_i}{(\phi_d + \phi_\tau)^2}. \tag{4.5b}$$

Equation (4.5) shows that η increases with $G(APE)$ but decreases when ϕ_τ increases. The numerators in (4.5a) and (4.5b) correspond to the two irreversible energy transfer rates in

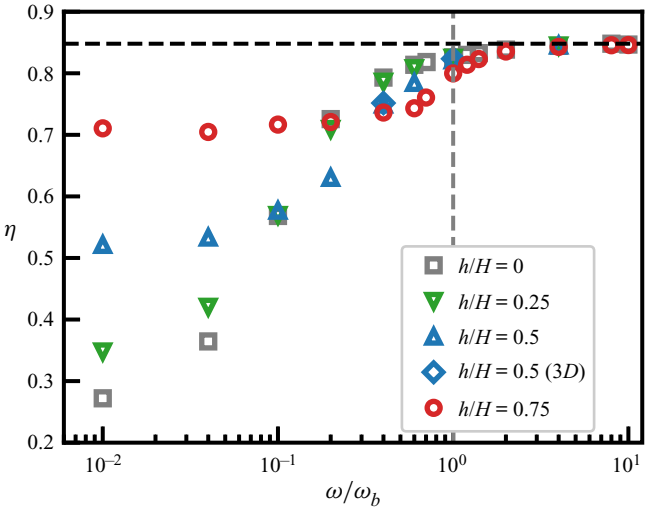

Figure 14. Mixing efficiency η as a function of ω/ω_b for different h/H. The horizontal dashed line represents the mixing efficiency in the absence of tide and topography, and the vertical dashed line represents $\omega/\omega_b = 1$.

this system and together form the denominator of η. As shown in figure 14, most of the results have $\eta > 0.5$, which implies that $\phi_d - \phi_i > \mathcal{E}$. Thus, (4.5) suggests that η is more sensitive to ϕ_τ than $G(APE)$. Furthermore, as shown in figures 5 and 8, both ϕ_τ and Nu increase as ω decreases, and note that Nu is proportional to $G(APE)$. One can further find that ϕ_τ is much more sensitive to the changes of ω than $G(APE)$ is. Recalling that η is more sensitive to ϕ_τ than $G(APE)$ and decreases as ϕ_τ increases, this explains the results that η decreases as ω decreases. We also observe at a certain range of ω in the tide-control regime ($\omega > \omega_b$), higher topography yields smaller η, which shows that global dissipation is more sensitive than $G(APE)$ (or Nu) to h/H as well. When ω decreases further, the system enters the drag-control regime. In this regime, both $G(APE)$ and ϵ_v become less sensitive to ω. As a result, η gradually stops decreasing with ω and asymptotically approaches to a saturated constant.

To better explain the results of mixing efficiency shown in figure 14, we present the results of the local mixing rate $\phi_d(x, z) = (\mathrm{d}z^*/\mathrm{d}\theta)|\nabla\theta|^2$ normalized by ϕ_d and local mixing efficiency (Sohail *et al.* 2018)

$$\eta_L \equiv \frac{\phi_d(x, z)}{\phi_d(x, z) + \epsilon_v(x, z)} \tag{4.6}$$

in figure 15. Figure 15(a) shows the normalized local mixing rate for $\omega = 0.4$, which corresponds to the buoyancy-control regime. Mixing is significant at two regions: one is the region underneath the cold plate, where plumes emit and generate downwelling flow; the other is the thermocline adjacent to the upper boundary. When the tidal frequency decreases to $\omega = 0.1$, which is the transitional frequency from the buoyancy-control to tide-control regime, we observe a tongue-like region with strong mixing near the topography, which is induced by the tide–topography interaction. Except for this point, the distribution of $\phi_d(x, z)/\phi_d$ is qualitatively similar to that of $\omega = 0.4$. We then compare figure 15(b,c), both of which correspond to the tide-control regime. One can find that the high-mixing regions underneath the cold plate and near topography extend as ω decreases, which suggests the increase of the global mixing rate. Such extension is stopped

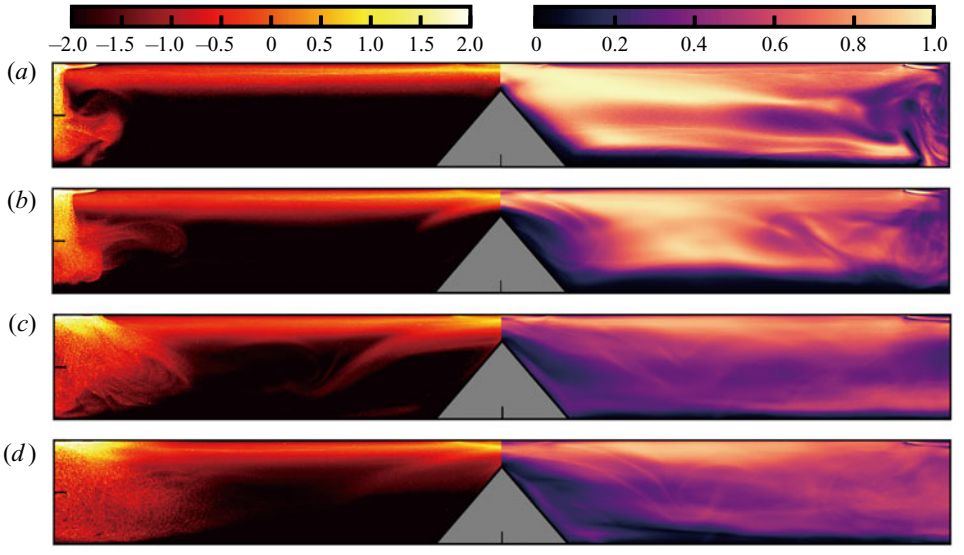

Figure 15. Temporal averaging of the normalized local mixing rate $\phi_d(x, z)/\phi_d$ in log scale (left half) and local mixing efficiency η_L (right half) for $h/H = 0.75$ and (*a*) $\omega = 0.4$, (*b*) 0.1, (*c*) 0.04 and (*d*) 0.01.

when the system enters the drag-control regime (see figure 15*d*). The results shown in figure 15 imply that in the tide-control regime, mixing is enhanced when ω decreases (U_{tide} increases); but in both the buoyancy- and drag-control regimes, mixing is insensitive to the change of ω. Recalling that Nu is proportional to $G(APE)$ and ϕ_d, this result is consistent with the observed Nu in figure 8. However, one should also be reminded that the enhancement in mixing does not mean an increase of the mixing efficiency. From the distribution of the local mixing efficiency η_L shown in figure 15(*e–h*), we can see that the η_L overall decreases as ω decreases in the right half of figure 15. This suggests that decreasing ω (increasing U_{tide}) induces a more significant enhancement in ϵ_v than ϕ_d, which is consistent with the results shown in figures 4, 8 and 14. In another word, the tidal force is more effective in driving than the mixing fluid.

As mixing in this system is sustained by two energy sources, the buoyancy and the tide, it may be illuminating to examine η in terms of the relative strength of the driving forces. The quantities that are related to the two types of energies are $G(APE)$ and ϕ_τ, respectively. We first rewrite (3.5) using (3.3):

$$\eta = \frac{G(APE) - \phi_i}{G(APE)} \frac{G(APE)}{G(APE) + \phi_\tau} = \eta' \frac{G(APE)}{G(APE) + \phi_\tau}, \tag{4.7}$$

where $\eta' = (G(APE) - \phi_i)/G(APE)$ is formally the same as the mixing efficiency for a classical HC system in the absence of tidal force. However, here in η', both ϕ_i and $G(APE)$ depend on ω. Because ϕ_i is small compared with $G(APE)$ for sufficiently large Ra (Peltier & Caulfield 2003; Gayen *et al.* 2013), η' asymptotically approaches its upper limit of 1 as Ra increases. For this reason, it is reasonable to neglect the ω-dependence in η' and we have $\eta' \approx \eta(\phi_\tau = 0) = \eta_{HC}$. Then, (4.7) can be simplified as

$$\eta \approx \frac{\eta_{HC}}{1 + \mathcal{R}}, \tag{4.8}$$

where $\mathcal{R} = \phi_\tau / G(APE)$. Equation (4.8) shows that for fixed Ra, the mixing efficiency can be expressed as a function of a single variable $\mathcal{R}$, which is the ratio of the mechanical

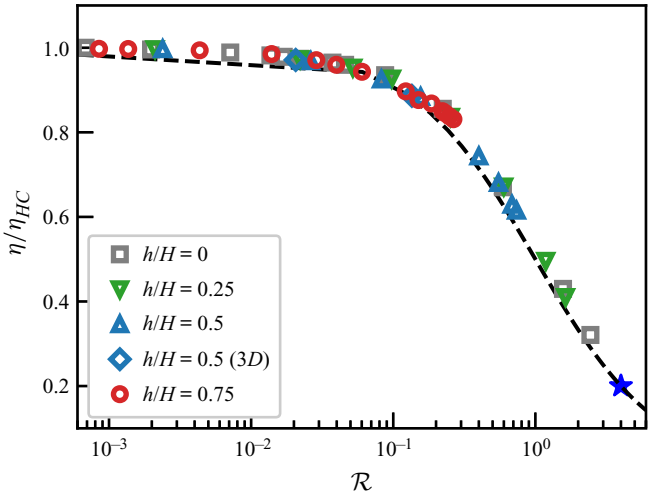

Figure 16. Graph of η/η_{HC} as a function of $\mathcal{R}$ for different h/H. The blue star refers to the oceanic estimation. Black dashed line represents $\eta/\eta_{HC} = 1/(1+\mathcal{R})$.

driving over the energy arising from the buoyancy. In the present study, the mechanical driving is in the form of tidal energy, but wind shearing and other forms of mechanical forcing can also be included in ϕ_τ. Figure 16 shows the normalized mixing efficiency η/η_{HC} as a function of $\mathcal{R}$. As shown in the figure, results for different h/H collapse on a single curve which can be well described by the function $1/(1+\mathcal{R})$ without any adjustable parameter (represented by the dashed line in the figure). The slight deviation of this curve from the data may be attributed to the weak ω dependence of η', which was neglected in obtaining (4.8).

Examining η in terms of $\mathcal{R}$ helps us to better understand the relationship between mixing and energy input. The generation rate of APE is estimated at 0.5 TW (Tailleux 2009), while tidal and wind driving individually contribute approximately 1 TW to the MOC (Munk & Wunsch 1998; Wunsch & Ferrari 2004). Because η_{HC} approaches 1 as Ra increases, it is reasonable to assume $\eta_{HC} \approx 1$ for the ocean, the Rayleigh number of which is up to 10^{26} (Sohail *et al.* 2018). Substituting these values into (4.8), we estimate the global mixing efficiency to be 0.2, which is consistent with the empirical value. The case for ocean interior is represented by the blue star in figure 16. Globally, to achieve a mixing efficiency down to 0.2, the system must be controlled by mechanical sources. However, by comparing results for different topographies, we wish to point out that the local mixing efficiency strongly depends on the local environment. Features like topography, latitude, local tidal forcing strength can all significantly affect the ratio of mechanical force over the buoyancy one. As a result, the mixing efficiencies of different locations can vary significantly. Looking at it in another way, whether at a specific location, the driving is dominated by mechanical or thermal sources can now be inferred from the local mixing efficiency. The mixing efficiency of the Southern Ocean is estimated to be approximately 0.75–0.80 (Sohail *et al.* 2018), which suggests that the thermal driving can be more important than the mechanical one in those locations. This result is consistent with the fact that the tidal currents are generally weak in the Southern Ocean (Poulain & Centurioni 2015).

We now discuss the behaviour of $\mathcal{R}$ as a function of ω, which is shown in figure 17. One sees that $\mathcal{R}$ has a similar dependence on ω as ϕ_τ shown in figure 5. For this reason, we fit

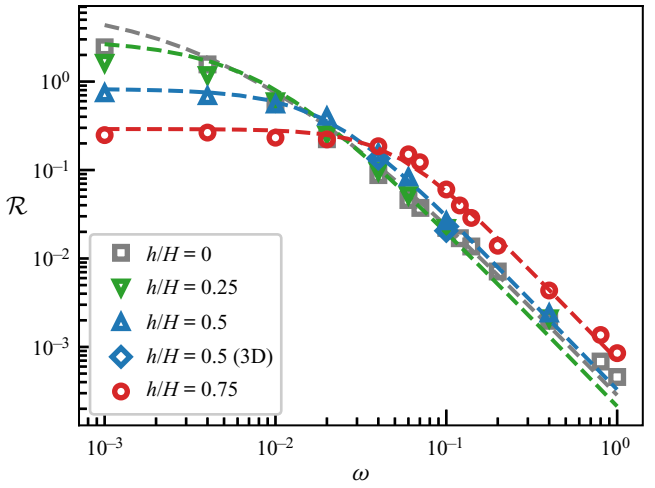

Figure 17. Graph showing $\mathcal{R}$ as a function of ω. The dashed curves correspond to the best fit of equation $\mathcal{R} = \mathcal{R}_\infty/(1 + B\omega + \omega^2/\omega_t^2)$.

$\mathcal{R}$ using a function similar to (4.2), i.e. $\mathcal{R} = \mathcal{R}_\infty/(1 + B\omega + \omega^2/\omega_t^2)$. The saturated value $\mathcal{R}_\infty$ of the energy ratio is the only fitting parameter here, because both B and ω_t are the same parameters that have been obtained in the fitting of (4.2) (see also figure 5). The best fits of this equation are shown as the dashed curves in figure 17. The fact that $\mathcal{R}$ and ϕ_τ can be described by a similar equation shows that $G(APE)$ has a relatively weak dependence on ω.

Figure 17 shows that for the tide- and buoyancy-control regimes with $\omega > \omega_t$, $\mathcal{R}$ follows a power law relationship ω^{-2}, and so we can write $\mathcal{R} \approx \mathcal{R}_\infty \omega_t^2/\omega^2 = \mathcal{R}_\infty Re_{tide}^2/Re_{tide}(\omega_t)^2$. Substitute this into (4.8), we obtain the following relation:

$$\gamma \equiv \frac{\eta}{\eta_{HC} - \eta} \approx \frac{1}{\mathcal{R}_\infty}\left(\frac{Re_{tide}}{Re_{tide}(\omega_t)}\right)^{-2} \quad (Re_{tide} < Re_{tide}(\omega_t)). \tag{4.9}$$

For sufficiently large values of Ra and high turbulence intensity, $\eta_{HC} \approx 1$ and the mixing efficiency η approximately equals the flux Richardson number R_f (Peltier & Caulfield 2003; Gregg *et al.* 2018). Thus, (4.9) can be written as

$$\gamma_{R_f} \equiv \frac{R_f}{1 - R_f} \approx \gamma \sim Re_{tide}^{-2}, \tag{4.10}$$

where γ_{R_f} is the mixing coefficient, which is an important parameter in ocean models used to estimate the diapycnal buoyancy flux and diapycnal diffusivity (Gregg *et al.* 2018). Equations (4.9) and (4.10) yield a scaling relation of the mixing coefficient $\gamma_{R_f} \sim Re_{tide}^{-2}$ in the tide- and buoyancy-control regimes. We plot γ as a function of Re_{tide}, and $\mathcal{R}_\infty\gamma$ as a function of $Re_{tide}/Re_{tide}(\omega_t)$ in figures 18(*a*) and 18(*b*), respectively. It shows that γ follows the scaling relationship $\gamma_{R_f} \sim Re_{tide}^2$ for $Re_{tide}/Re_{tide}(\omega_t) < 1$. However, as shown in 18(*a*), most of our cases have magnitudes much larger than the mixing coefficient γ_{R_f} of the ocean, which is usually less than one (Gregg *et al.* 2018). This discrepancy with the field observation may be attributed to the limited parameter range of the current study. One of the consequences is that the approximation $\gamma_{HC} \approx 1$ may not hold for limited Ra. In fact, for the Rayleigh number we used in this study ($Ra = 1 \times 10^{10}$), we

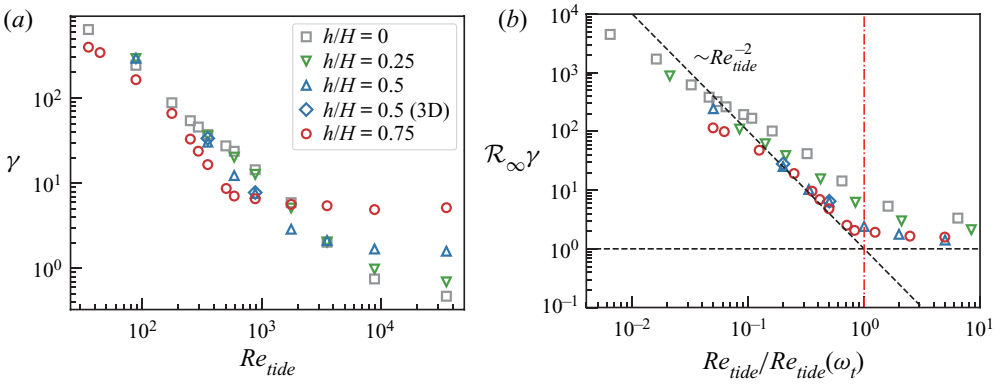

Figure 18. Graph showing (*a*) γ and (*b*) $\mathcal{R}_\infty\gamma$ as a function of $Re_{tide}/Re_{tide}(\omega_t)$ for different h/H. In panel (*b*), the inclined black dashed line represents $[Re_{tide}/Re_{tide}(\omega_t)]^{-2}$, and the red dash–dotted line refers to $Re_{tide} = Re_{tide}(\omega_t)$.

obtain $\gamma_{HC} = 0.85$, which is probably not sufficiently close to 1. Another consequence is related to the magnitude of η. Considering the transitional state between the buoyancy- and tide-control regimes where the flow strengths driven by tidal and surface thermal forcings are comparable (i.e. Re_{tide} equals to the Reynolds number in a classical HC system in the absence of tide), because the tidal force does not greatly enhance the heat transfer, one can estimate $G(APE)$ according to the power law relationship of Nu for a classical HC system as $G(APE) \sim Nu \sim Ra^{0.2}$ (Rossby 1965; Shishkina *et al.* 2016). In a classical HC system, the Reynolds number has a scaling relationship $Re \sim Ra^{0.4}$ (Mullarney *et al.* 2004). Because the tidal velocity is comparable to the background flow, one can obtain $\phi_\tau \sim Re_{tide}^2 \sim Ra^{0.8}$. One can find that the tidal power increases much faster than $G(APE)$ as Ra increases. As a result, the mixing efficiency η will decrease and yields a value of γ closer to the mixing coefficient of the ocean γ_{R_f}. Thus, we expect that γ will be closer to γ_{R_f} for higher Ra, and examining the power law relationship (4.10) in simulations or experiments with higher Ra could be one of the goals in future studies.

It is seen from figure 18 that for large Re_{tide} and for some cases with $h/H = 0$ and 0.25, the value of γ can be smaller than 1, which is in the range of γ_{R_f} observed in the ocean. However, we cannot thus draw the conclusion that the ocean is within the drag-control regime. To see this, we estimate the typical ocean current speed by first assuming a buoyancy driven background flow. The flow strength in such a case is given by $Re = CRa^{0.4}$, where C is a constant to be determined. Using the value of Re in the absence of topography and tidal force, we determine the constant $C = 0.034$. Thus, when buoyancy is the only energy source, the velocity of the thermocline is given by $U_{thermo} \approx CRa^{-0.1}\sqrt{\alpha g L \Delta Pr}$. We take $g = 9.8$ m s^{-2}, $\alpha = 1 \times 10^{-4}$ K^{-1} (Sohail *et al.* 2018), $L = 1 \times 10^7$ m, $\Delta = 10$ K, $\kappa = 1 \times 10^{-7}$ m^2 s^{-1} and $\nu = 1 \times 10^{-6}$ m^2 s^{-1} (Siggers, Kerswell & Balmforth 2004). Thence, we estimate $U_{thermo} \approx 2$ cm s^{-1} if the ocean current is driven by thermal forcing. As for the tidal current, the Global Drifter Program (GDP) data shows that the M2 (semidiurnal) currents in the open-ocean areas are 3–5 cm s^{-1} (Poulain & Centurioni 2015), which suggests that the tide is the dominant energy source in such areas of the ocean. However, in the deep tropics and South Pacific,

for example, the M2 currents are small (< 2 cm s^{-1}). Thus, in these areas, buoyancy could be the dominant governing mechanism.

5. Conclusion

We have made a numerical study of horizontal convection with tidal force and topography. Our results show that viscous dissipation of this system strongly depends on ω. As a result of tide–topography interaction, local dissipation near the topography will be enhanced when the tide is sufficiently strong. Such enhancement is proportional to the height of the topography. In the bulk region, the enhancement of dissipation is less than that in regions adjacent to a topography. When ω is smaller than a certain frequency ω_t, the enhancement becomes less sensitive to ω and the global viscous dissipation asymptotically approaches to a constant. We name this the drag-control regime, which means that the tidal force is balanced by the viscous drag. As a result, the kinetic energy will not increase further as ω decreases. For higher topography, ω_t is larger, which corresponds to smaller tidal velocity U_{tide}, and the saturated constant is also smaller. This implies that topography not only enhances local dissipation, through tide–topography interaction, but may also hinder the flow from accelerating by the tidal force. By separating the velocity into parts governed by the tidal force and buoyancy, and comparing the magnitudes of these parts, two regimes, the tide- and buoyancy-control regimes, can be identified. In the buoyancy-control regime, the flow strength is determined by the surface thermal forcing. However, fluid is accelerated by tidal force. When the flow strength driven by tide is stronger than that by buoyancy, the system enters the tide-control regime. We find that both the global dissipation and heat transfer rate are enhanced when the system is in the tide-control regime.

The simulations conducted in this study and the corresponding flow regimes are shown in the phase diagram shown in figure 19. According to the corresponding governing mechanisms, the phase diagram is divided into three regions: buoyancy-control (grey coloured), tide-control (blue coloured) and drag-control (orange coloured) regions. The vertical blue dashed line separating buoyancy- and tide-control regimes represents $Re_{tide} = Re_{tide}(\omega_b)$. As shown in the above, for the buoyancy-control regime ($Re_{tide} < Re_{tide}(\omega_b)$), the global features of the system, for example, the global dissipation and heat transfer rate, are not sensitive to the topography, as demonstrated in figures 4 and 8. Thus, the transitional Reynolds number $Re_{tide}(\omega_b)$ has no topography dependence. The orange dashed line separating the tide- and drag-control regimes represents $Re_{tide} = Re_{tide}(\omega_t)$. The transition from tide to drag control is determined by the strength of the viscous drag, which is proportional to the flow strength represented by Re_{tide}. As Re_{tide} increases, the viscous drag becomes comparable to the tidal force and the system enters the drag-control regime. For higher topography, this process occurs at smaller values of Re_{tide}, because not only the viscous drag but also the blockage effect from the topography will hinder the flow from accelerating.

A parameter $\mathcal{R}$ is introduced, which represents the ratio between tidal and potential energy injections. We have demonstrated that for sufficiently large Ra, the mixing efficiency η only depends on the energy ratio $\mathcal{R}$. According to the global energy input to the ocean interior, we provide an estimate of the global mixing efficiency of 0.2, which is consistent with the empirical value. We note that because the energy ratio $\mathcal{R}$ strongly depends on the local environment, the mixing efficiency at specific locations can be outside of the range given above. We further find that this energy ratio $\mathcal{R}$ has a similar

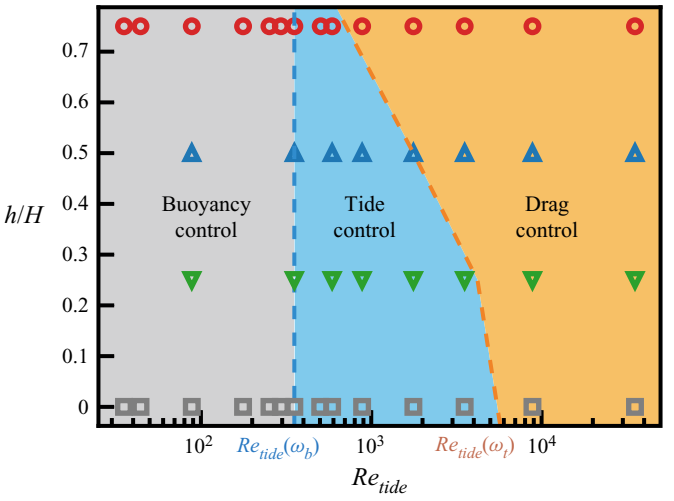

Figure 19. Phase diagram based on $Ra = 1 \times 10^{10}$ and $Pr = 8.0$. The symbols represent the cases of different topographies in this study. Buoyancy-, tide- and drag-control regimes are shown in grey, blue and orange, respectively. The blue dashed line separating the buoyancy- and tide-control regimes corresponds to $Re_{tide} = Re_{tide}(\omega_b) \sim Ra^{0.4}$, which equals the Reynolds number of a classical HC system in the absence of tidal force (Mullarney *et al.* 2004). The orange dash line separating the tide- and drag-control regimes corresponds to $Re_{tide} = Re_{tide}(\omega_t)$.

behaviour as the tidal power ϕ_τ. We estimate the typical velocity of the thermocline if buoyancy is the only energy source, and demonstrate that the governing mechanism in a certain ocean region depends on the relative strength of the local tidal and buoyancy forcings. For the tide- and buoyancy-control regimes, we further derive a relationship $\gamma_{R_f} \sim Re_{tide}^2$, which connects the mixing coefficient and the tidal Reynolds number. We expect that for higher Ra, our results will be closer to realistic ocean values, which will be interesting to examine in future studies.

Finally, we remark that in this study, we focus on the global energy balance of the system. Owing to the neglect of Coriolis force and some other important features in the ocean, one should bear in mind that the local properties observed here could be different from the real ocean. Nevertheless, the relationships of global energy balance and regime separation proposed in this study may contribute to the understanding of the MOC dynamics.

Acknowledgements. The authors would like to thank Y.-B. Hu and F. Wang for stimulating discussions. Numerical resources of this study are supported by Center for Computational Science and Engineering at Southern University of Science and Technology.

Funding. This work is supported by the National Natural Science Foundation of China (Grant No. 12072144); the Research Grants Council of HKSAR (Grant Nos CUHK14301115 and CUHK14302317); and the Department of Science and Technology of Guangdong Province (Grant No. 2019B21203001).

Declaration of interests. The authors report no conflict of interest.

Author ORCIDs.
Guang-Yu Ding https://orcid.org/0000-0001-8636-9738;
Ke-Qing Xia https://orcid.org/0000-0001-5093-9014.

References

Bretherton, F.P. 1966 The propagation of groups of internal gravity waves in a shear flow. *Q. J. R. Meteorol. Soc.* **92** (394), 466–480.

Caldwell, D.R. & Mourn, J.N. 1995 Turbulence and mixing in the ocean. *Rev. Geophys.* **33** (2 S), 1385–1394.

Chong, K.-L., Ding, G. & Xia, K.-Q. 2018 Multiple-resolution scheme in finite-volume code for active or passive scalar turbulence. *J. Comput. Phys.* **375**, 1045–1058.

Egbert, G.D. & Ray, R.D. 2000 Significant dissipation of tidal energy in the deep ocean inferred from satellite altimeter data. *Nature* **405** (6788), 775–778.

Fadlun, E.A., Verzicco, R., Orlandi, P. & Mohd-Yusof, J. 2000 Combined immersed-boundary finite-difference methods for three-dimensional complex flow simulations. *J. Comput. Phys.* **161** (1), 35–60.

Garrett, C. & Kunze, E. 2007 Internal tide generation in the deep ocean. *Annu. Rev. Fluid Mech.* **39** (1), 57–87.

Gayen, B., Griffiths, R.W., Hughes, G.O. & Saenz, J.A. 2013 Energetics of horizontal convection. *J. Fluid Mech.* **716**, R10.

Gregg, M.C., D'Asaro, E.A., Riley, J.J. & Kunze, E. 2018 Mixing efficiency in the ocean. *Annu. Rev. Mar. Sci.* **10** (1), 443–473.

Hazewinkel, J., Paparella, F. & Young, W.R. 2012 Stressed horizontal convection. *J. Fluid Mech.* **692**, 317–331.

Heywood, K.J., Naveira Garabato, A.C. & Stevens, D.P. 2002 High mixing rates in the abyssal Southern Ocean. *Nature* **415** (6875), 1011–1014.

Huang, R.X. 1999 Mixing and energetics of the oceanic thermohaline circulation. *J. Phys. Oceanogr.* **29** (4), 727–746.

Hughes, G.O. & Griffiths, R.W. 2008 Horizontal convection. *Annu. Rev. Fluid Mech.* **40** (1), 185–208.

Hughes, G.O., Hogg, A.M. & Griffiths, R.W. 2009 Available potential energy and irreversible mixing in the meridional overturning circulation. *J. Phys. Oceanogr.* **39** (12), 3130–3146.

Kaczorowski, M., Chong, K.-L. & Xia, K.-Q. 2014 Turbulent flow in the bulk of Rayleigh–Bénard convection: aspect-ratio dependence of the small-scale properties. *J. Fluid Mech.* **747**, 73–102.

Kaczorowski, M. & Xia, K.-Q. 2013 Turbulent flow in the bulk of Rayleigh–Bénard convection: small-scale properties in a cubic cell. *J. Fluid Mech.* **722**, 596–617.

Killworth, P.D. & Manins, P.C. 1980 A model of confined thermal convection driven by non-uniform heating from below. *J. Fluid Mech.* **98** (03), 587–607.

Kuhlbrodt, T., Griesel, A., Montoya, M., Levermann, A., Hofmann, M. & Rahmstorf, S. 2007 On the driving processes of the Atlantic meridional overturning circulation. *Atlantic* **45** (2004), RG2001.

Kundu, P.K., Cohen, I.M. & Dowling, D.R. 2016 *Fluid Mechanics*, 6th edn, pp. 349–407. Academic.

Lamb, K.G. 2014 Internal wave breaking and dissipation mechanisms on the continental slope/shelf. *Annu. Rev. Fluid Mech.* **46** (1), 231–254.

Ledwell, J.R., Montgomery, E.T., Polzin, K.L., St. Laurent, L.C., Schmitt, R.W. & Toole, J.M. 2000 Evidence for enhanced mixing over rough topography in the abyssal ocean. *Nature* **403** (6766), 179–182.

Li, G., Cheng, L., Zhu, J., Trenberth, K.E., Mann, J.E. & Abraham, J.P. 2020 Increasing ocean stratification over the past half-century. *Nat. Clim. Change* **10** (12), 1116–1123.

Lorenz, E.N. 1955 Available potential energy and the maintenance of the general circulation. *Tellus* **7** (2), 157–167.

Mashayek, A., Ferrari, R., Vettoretti, G. & Peltier, W.R. 2013 The role of the geothermal heat flux in driving the abyssal ocean circulation. *Geophys. Res. Lett.* **40** (12), 3144–3149.

Mathur, M. & Peacock, T. 2009 Internal wave beam propagation in non-uniform stratifications. *J. Fluid Mech.* **639**, 133–152.

Monismith, S.G., Koseff, J.R. & White, B.L. 2018 Mixing efficiency in the presence of stratification: when is it constant? *Geophys. Res. Lett.* **45** (11), 5627–5634.

Mullarney, J.C., Griffiths, R.W. & Hughes, G.O. 2004 Convection driven by differential heating at a horizontal boundary. *J. Fluid Mech.* **516**, 181–209.

Munk, W. & Wunsch, C. 1998 Abyssal recipes II: energetics of tidal and wind mixing. *Deep-Sea Res.* **45** (12), 1977–2010.

Munk, W.H. 1966 Abyssal recipes. *Deep-Sea Res.* **13** (4), 707–730.

Nycander, J. 2005 Generation of internal waves in the deep ocean by tides. *J. Geophys. Res.* **110** (10), 1–9.

Paparella, F. & Young, W.R. 2002 Horizontal convection is non-turbulent. *J. Fluid Mech.* **466**, 205–214.

PELTIER, W.R. & CAULFIELD, C.P. 2003 Mixing efficiency in stratified shear flows. *Annu. Rev. Fluid Mech.* **35** (1), 135–167.

POLZIN, K.L., TOOLE, J.M., LEDWELL, J.R. & SCHMITT, R.W. 1997 Spatial variability of turbulent mixing in the abyssal ocean. *Science* **276** (5309), 93–96.

POULAIN, P.-M. & CENTURIONI, L. 2015 Direct measurements of World Ocean tidal currents with surface drifters. *J. Geophys. Res.* **120** (10), 6986–7003.

ROSSBY, H.T. 1965 On thermal convection driven by non-uniform heating from below: an experimental study. *Deep-Sea Res.* **12** (1), 9–16.

SAENZ, J.A., HOGG, A.M., HUGHES, G.O. & GRIFFITHS, R.W. 2012 Mechanical power input from buoyancy and wind to the circulation in an ocean model. *Geophys. Res. Lett.* **39** (13), L13605.

SALEHIPOUR, H. & PELTIER, W.R. 2015 Diapycnal diffusivity, turbulent Prandtl number and mixing efficiency in Boussinesq stratified turbulence. *J. Fluid Mech.* **775** (May), 464–500.

SARKAR, S. & SCOTTI, A. 2017 From topographic internal gravity waves to turbulence. *Annu. Rev. Fluid Mech.* **49** (1), 195–220.

SCOTT, J.R., MAROTZKE, J. & ADCROFT, A. 2001 Geothermal heating and its influence on the meridional overturning circulation. *J. Geophys. Res.* **106** (C12), 31141–31154.

SCOTTI, A. & WHITE, B. 2011 Is horizontal convection really non-turbulent? *Geophys. Res. Lett.* **38** (21), L21609.

SHISHKINA, O. 2017 Mean flow structure in horizontal convection. *J. Fluid Mech.* **812**, 525–540.

SHISHKINA, O., GROSSMANN, S. & LOHSE, D. 2016 Heat and momentum transport scalings in horizontal convection. *Geophys. Res. Lett.* **43** (3), 1219–1225.

SIGGERS, J.H., KERSWELL, R.R. & BALMFORTH, N.J. 2004 Bounds on horizontal convection. *J. Fluid Mech.* **517**, 55–70.

SMYTH, W.D. & MOUM, J.N. 2000 Length scales of turbulence in stably stratified mixing layers. *Phys. Fluids* **12** (6), 1327–1342.

SOHAIL, T., GAYEN, B. & HOGG, A.M.C. 2018 Convection enhances mixing in the Southern Ocean. *Geophys. Res. Lett.* **45** (9), 4198–4207.

TAILLEUX, R. 2009 On the energetics of stratified turbulent mixing, irreversible thermodynamics, Boussinesq models and the ocean heat engine controversy. *J. Fluid Mech.* **638**, 339–382.

WANG, F., HUANG, S.-D. & XIA, K.-Q. 2018 Contribution of surface thermal forcing to mixing in the ocean. *J. Geophys. Res.* **123** (2), 855–863.

WANG, F., HUANG, S.-D., ZHOU, S.-Q. & XIA, K.-Q. 2016 Laboratory simulation of the geothermal heating effects on ocean overturning circulation. *J. Geophys. Res.* **121** (10), 7589–7598.

WANG, W. & HUANG, R.X. 2005 An experimental study on thermal circulation driven by horizontal differential heating. *J. Fluid Mech.* **540**, 49–73.

WATERHOUSE, A.F., *et al.* 2014 Global patterns of diapycnal mixing from measurements of the turbulent dissipation rate. *J. Phys. Oceanogr.* **44** (7), 1854–1872.

WHITEHEAD, J.A. 1995 Thermohaline ocean processes and models. *Annu. Rev. Fluid Mech.* **27** (1), 89–113.

WINTERS, K.B., LOMBARD, P.N., RILEY, J.J. & D'ASARO, E.A. 1995 Available potential energy and mixing in density-stratified fluids. *J. Fluid Mech.* **289**, 115–128.

WINTERS, K.B. & YOUNG, W.R. 2009 Available potential energy and buoyancy variance in horizontal convection. *J. Fluid Mech.* **629**, 221–230.

WUNSCH, C. 2000 Moon, tides and climate. *Nature* **405** (6788), 743–744.

WUNSCH, C. & FERRARI, R. 2004 Vertical mixing, energy, and the general circulation of the oceans. *Annu. Rev. Fluid Mech.* **36** (1), 281–314.